Fall 1997

An experimental investigation of thermally-induced deformation of 1 micron thick copper/tantalum/polymide high-density interconnect structures

Dmitry V. Zhmurkin
University of New Hampshire, Durham

Recommended Citation

INFORMATION TO USERS

This manuscript has been reproduced from the microfilm master. UMI films the text directly from the original or copy submitted. Thus, some thesis and dissertation copies are in typewriter face, while others may be from any type of computer printer.

The quality of this reproduction is dependent upon the quality of the copy submitted. Broken or indistinct print, colored or poor quality illustrations and photographs, print bleedthrough, substandard margins, and improper alignment can adversely affect reproduction.

In the unlikely event that the author did not send UMI a complete manuscript and there are missing pages, these will be noted. Also, if unauthorized copyright material had to be removed, a note will indicate the deletion.

Oversize materials (e.g., maps, drawings, charts) are reproduced by sectioning the original, beginning at the upper left-hand corner and continuing from left to right in equal sections with small overlaps. Each original is also photographed in one exposure and is included in reduced form at the back of the book.

Photographs included in the original manuscript have been reproduced xerographically in this copy. Higher quality 6" x 9" black and white photographic prints are available for any photographs or illustrations appearing in this copy for an additional charge. Contact UMI directly to order.

UMI

AN EXPERIMENTAL INVESTIGATION OF THERMALLY INDUCED
DEFORMATION OF 1 MICRON THICK
COPPER/TANTALUM/POLYIMIDE
HIGH DENSITY INTERCONNECT STRUCTURES

BY

DMITRY V. ZHMURKIN
B.S.M.E. Moscow State University, Russia, 1992

DISSERTATION

Submitted to the University of New Hampshire
in Partial Fulfillment of
the Requirements for the Degree of

Doctor of Philosophy

in

Engineering

September 1997

UMI
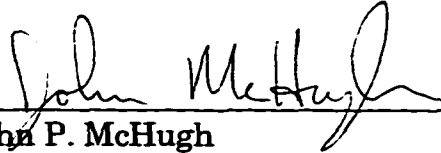
This dissertation has been examined and approved
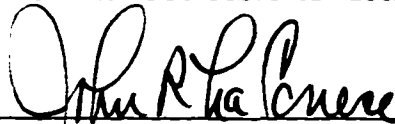
Dissertation Director, Todd S. Gross
Professor of Mechanical Engineering

James E. Krzanowski
Associate Professor of Mechanical Engineering

John P. McHugh
Associate Professor of Mechanical Engineering

Andrzej Rucinski
Professor of Electrical and Computer Engineering,
Institute for the Study of Earth, Oceans, and Space

M. Robinson Swift
Professor of Mechanical Engineering

8/25/97
Date

ACKNOWLEDGEMENTS

The author would like to thank Paivikki Buchwalter from IBM T.J. Watson Research Center for her support and helpful discussions, Michael Chen, Kapil Sheth and Professor R. Farris of the University of Massachusetts, Department of Polymer Science and Engineering for sharing their data on the elastic properties of the polyimides. Marc Czapczynski is also acknowledged for his Atomic Force Microscope viewer program that simplified many data acquisition tasks. My deepest thanks and gratitude go to Professor Todd Gross for his tremendous constant guidance and support, and enthusiasm that was essential to the completion of this work.

iii

TABLE OF CONTENTS

v

LIST OF FIGURES

LIST OF ABBREVIATIONS

AFM .... Atomic Force Microscope

CMOS .... Complementary Metal Oxide Semiconductor

CMP .... Chemical-Mechanical Polishing

CTE .... Coefficient of Thermal Expansion

Cu .... Copper

CVD .... Chemical Vapor Deposition

FEA .... Finite Element Analysis

HDIC .... High Density Interconnect

LASSI .... Laser Spot Scanning Interferometry

PSPD .... Position-Sensitive Photodetector

ppm/°C .... 10^6 °C^{-1} (for example, 5 ppm/°C = 5 x 10^6 °C^{-1})

PZT .... Piezoelectric Transducer

RIE .... Reactive Ion Etching

Si .... Silicon

SRAM .... Static Random Access Memory

SPM .... Scanning Probe Microscope

SEM .... Scanning Electron Microscope

STM .... Scanning Tunneling Microscope

Ta .... Tantalum

TEM .... Transmission Electron Microscope

ABSTRACT

AN EXPERIMENTAL INVESTIGATION OF THERMALLY INDUCED DEFORMATION OF 1 MICRON THICK COPPER/TANTALUM/POLYIMIDE HIGH DENSITY INTERCONNECT STRUCTURES
by
Dmitry Zhmurkin
University of New Hampshire, September 1997

A new technique to estimate the out-of-plane thermal expansion coefficient (CTE) of several 1 μm thick, spin-coated polyimides is introduced. Arrays of parallel copper and polyimide lines of various aspect ratios on Si substrate were imaged in air at room temperature and at 97 °C using an atomic force microscope (AFM). The out-of-plane CTE of the polyimides was estimated by matching the experimental results with the predictions of finite element models with different out-of-plane parameters. For FPI-135 (6FCDA-TMOB) polyimide the out-of-plane CTE was found to be $\approx$ 260 ppm/°C, for FPI-136 (PMDA-6FDA-TFMOB) polyimide $\approx$ 120 ppm/°C. Polyimide lines with widths equal to or less than the film thickness of 1 μm showed less thermal expansion than wider lines. This was attributed to change of polyimide properties at the Cu/polyimide interface as a result of the reactive ion etching step of the structure manufacturing process.

High density interconnect structures are subjected to 350 °C during manufacturing. The mismatch between the Cu and the polyimide out-of-plane CTE leads to high shear stresses at the interfaces normal to the film plane during heating. The experimental observation of thermally induced deformation of Cu/Ta/polyimide line arrays as a result of RT-350°C-RT thermal cycle is discussed. In addition to "classical" high temperature deformation mechanisms (grain boundary sliding, grain elevation and Coble creep on the Cu surface), sliding at the Cu/Ta interface was observed using the AFM. It was found that the Cu/Ta interfacial sliding is a strong function of the Cu line width. 10 μm wide Cu lines were found to exhibit less Cu/Ta sliding compared to 1 μm wide Cu lines. This was attributed to ability of wide Cu lines relax the stresses using other mechanisms. A finite element model was constructed to analyze the Cu/Ta interfacial sliding.

xi

CHAPTER 1

INTRODUCTION

1.1. Modern Trends in On-Chip Wiring Technology for VLSI

Very Large Scale Integration (VLSI) is the key to the continuing development in the computer industry.[1] Its implementation depends upon fabricating and interconnecting the increasing numbers of components on silicon chips. As VLSI structures are scaled to smaller dimensions, fabrication becomes more complex, but the increasing requirements of speed of signal propagation, processing costs, and reliability are being transferred from the active semiconductor devices to the on-chip interconnections. Increased integration leads to the need for greater numbers of wiring levels for semiconductor devices. More wiring levels result in an increased number of processing operations and in more complex manufacturing methods. Increased current densities in the finer dimensions and the submicron dimension of the structures lead to increased concern for reliability. In combination, these requirements result in a need for the more effective material systems for high-speed performance in interconnecting devices. This is why new conductive and dielectric materials are being considered for use in more reliable, high-performance interconnects.

1

1.1-1. Types of interconnections

The functions served by the interconnections can be divided into four parts.[1] The first of these, called local interconnections, are used to wire active devices and passive elements into a circuit element. These circuit elements may be storage nodes of static random access memory device or logic elements. A second type of interconnection, referred to as global wiring, is used to connect circuit elements. The most demanding use of these "wires" occurs in logic arrays, where such connections may span the full extent of the chip. It is these longest lines on a chip, which limit its overall speed. The interconnections of the third type carry power to the active devices on the chip. Finally, there are interconnects that act as an interface with the packaging element on which the chips are mounted and interconnected. This interface may be either bonding pads or an array of solder bumps, which can be joined to a similar array on the packaging element. This final level of wiring usually combines this latter function with a primary distribution of power. As dimensions are reduced, the relative importance of each of these different wiring functions to chip performance, to processing cost and to overall reliability increases. Two examples of multilevel interconnect structures, showing local and global interconnects are given in Figure 1-1 and Figure 1-2.

2
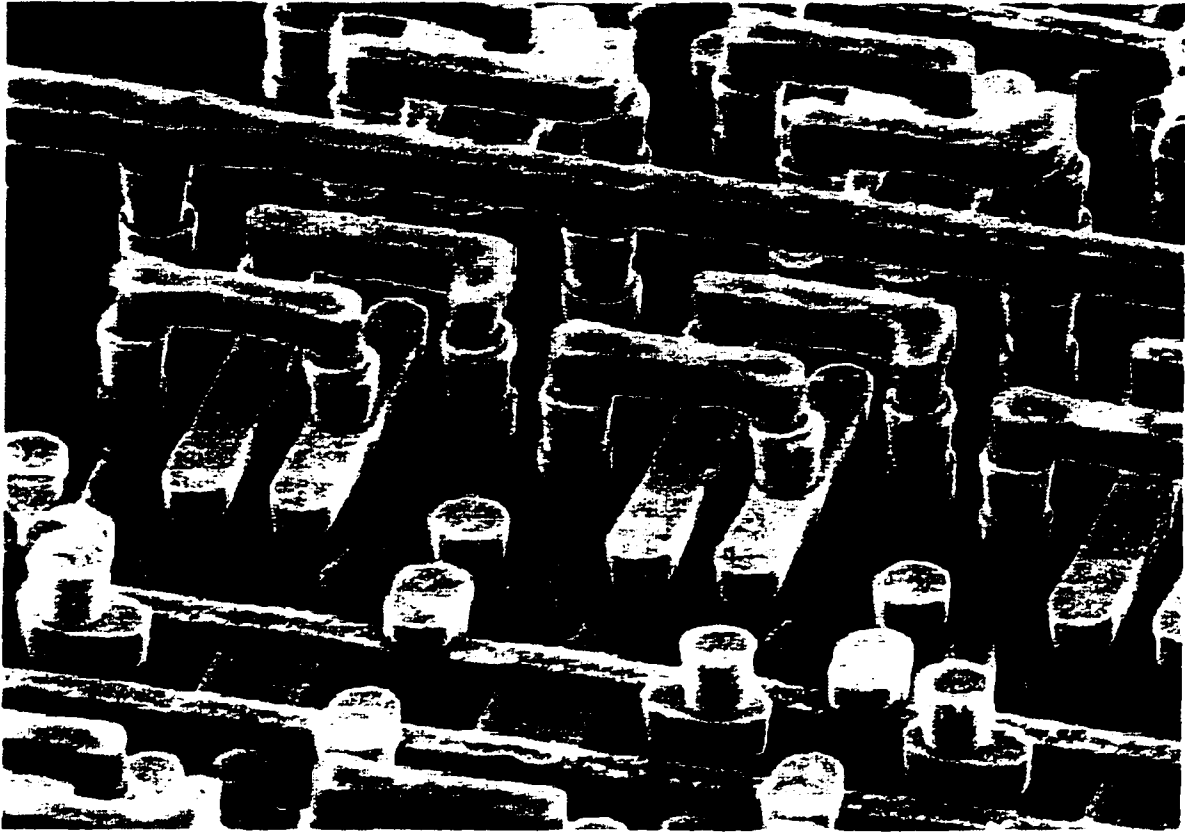
Figure 1-1. Low-angle scanning electron micrograph of a portion of a SRAM array. The insulating dielectric has been removed, revealing the lower levels of the interconnection structure of the array. The local interconnections (tungsten; colored pink) provide cross-coupling for the n^+ and p^+ diffusion contacts and act as the lower portions of the contact studs to the first global interconnection level (Ti/Al(Cu)/Ti/TiN; colored yellow). The contact studs (tungsten; colored light green) constitute the upper portions of the contact paths to the global interconnections. (Copyright 1995 IBM Corporation. Reprinted with permission from *IBM Journal of Research and Development*, Vol. 39, No. 4)

3
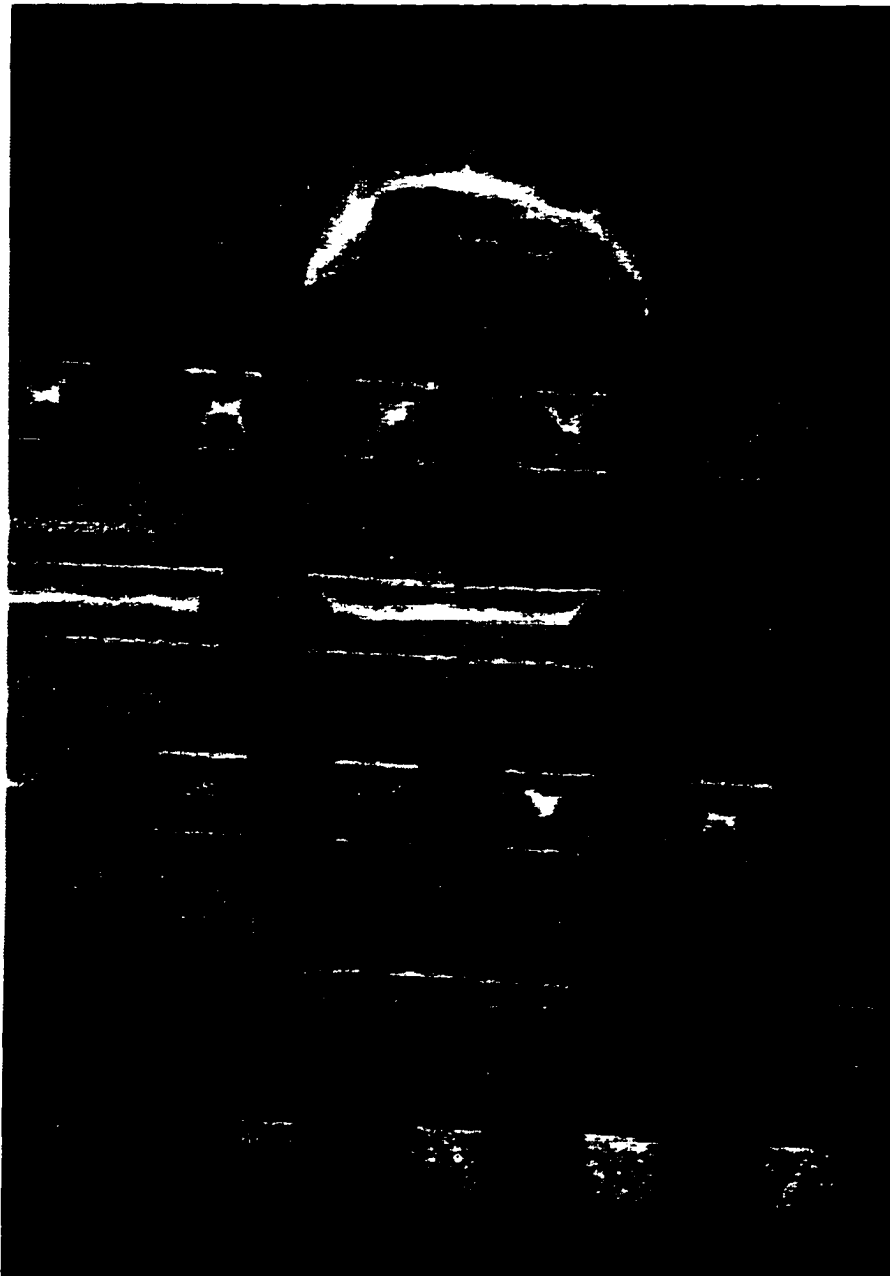
Figure 1-2. Scanning electron micrograph cross section of a portion of a 0.5-
μm CMOS logic chip currently in production. Note that a local interconnect
level and five global interconnect levels are used. (Copyright 1995 IBM
Corporation. Reprinted with permission from *IBM Journal of Research and
Development*, Vol. 35, No. 1/2)

4

1.1-2. Need for an improved material system for interconnections

Improvements in the performance of on-chip wiring structures require consideration of new conductors with lower resistivity and new insulators with lower dielectric constant than currently used materials, without compromising the increasing demands for reliability and yield.[2] The materials commonly used today are SiO_2 as dielectrics and aluminum-based alloys as conductors. The 2.7 $\mu\Omega$-cm resistivity of pure aluminum is not actually obtained in current interconnections, since aluminum is alloyed with copper to increase its resistance to electromigration and stress-induced migration, and/or silicon to minimize its contact reaction with silicon devices. A typical resistivity for Al-0.5 wt.% Cu (aluminum alloy, containing 0.5 weight percent of copper) is 3.0 - 3.2 $\mu\Omega$-cm. The low resistivity of copper (1.7 $\mu\Omega$-cm at 22 °C) is its prime advantage in replacing aluminum alloys for chip interconnections. The need for reduced capacitance and resistance of interconnects has stimulated activity to identify new low dielectric constant insulators with the right properties for integration with Cu. The dielectric constant must be substantially lower than that of amorphous SiO_2. Silicon dioxide has a dielectric constant of about 3.9; this is one of the lowest among common inorganic materials. Polyimides can be prepared with a range of dielectric constants (the lowest being about 2.3), with the possibility of further reductions. During the development of Cu/polyimide structures, it

5

was shown that the dielectric constant ε of BPDA-PDA[†] polyimide is highly anisotropic, with $\varepsilon = 2.9$ out-of-plane and $\varepsilon = 3.7$ in-plane.[3,4]

Potential concerns with polymeric materials are their absorption of water or processing chemicals and their mechanical properties. Polymers are more readily deformed by stress than inorganic dielectrics; however, they are not as brittle. The mechanical properties of organic and inorganic insulators differ greatly. At the temperatures encountered during fabrication and use of interconnection structures, amorphous SiO_2 is a rigid, brittle material compared with aluminum or copper. The differences in thermal expansion coefficients produce high tensile stress at room temperature in metals after thermal cycling in SiO_2 insulation. In contrast, organic materials (e.g. polyimides) have lower Young's modulus, but much greater elongation in break than SiO_2. Also, the mechanical properties of some polyimides are highly anisotropic in terms of measurements parallel or perpendicular to the plane of the wafer. For example, for BPDA-PDA,[5] the in-plane coefficient of thermal expansion (CTE) varies from 5 ppm/°C at 20 °C to 10 ppm/°C at 400 °C, while the out-of-plane coefficient varies from 100 ppm/°C at 20 °C to 400 ppm/°C at 400 °C, increasing rapidly above 300 °C.

_____

[†] BPDA=3,3'4,4'-biphenyl dianhydride

6

1.1-3. High density interconnect fabrication process

Modern technology involved in manufacturing process of planar multilevel High Density Interconnects (HDIC) was introduced in the computer industry around 1988, and since then it has been improving[6] to provide the current advances in microelectronics. Now it combines lithographic techniques with Chemical Vapor Deposition (CVD) and Chemical-Mechanical Polishing (CMP) to achieve planar, multilevel metallization architectures. A schematic of a damascene manufacturing process of single-level copper-polyimide interconnect structure is shown in Figure 1-3. First, a polyamic acid is spin-coated on a 0.5 mm thick silicon substrate. It is cured at 350 °C in nitrogen to form a 1 μm thick polyimide film. Second, a 100 nm thick Si_3N_4 cap is deposited on top of the polyimide at elevated temperature, which is used as a stop layer for the polishing. Then, the system is coated with photoresist and the pattern is exposed to UV light. Unexposed photoresist is removed by developer and the exposed silicon nitride and polyimide are etched out by Reactive Ion Etching (RIE). After this a 30-200 nm thick Ta liner is deposited on the structure at elevated temperature. This layer is used to improve Cu adhesion to the insulator and to prevent Cu diffusion into the Si and the dielectric.[2] Then a Cu film is deposited. Several metal deposition techniques have been utilized for filling the trenches or vias, such as collimated sputtering, ion cluster beam, electron cyclotron resonance, CVD, electroless and electrolytic plating depositions. Using chemical-mechanical methods,

7

1. Spin coat 1 μm thick polyimide layer at room temperature. Cure at 350°C

2. Deposit 100 nm thick silicon nitride cap at elevated temperature.

UV light
Glass Plate
Photoresist

3. Deposit and cure photoresist. Expose pattern.
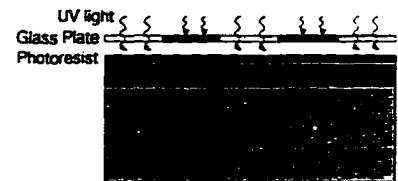
4. Develop photoresist and ion etch unexposed polyimide. Remove exposed photoresist.

5. Deposit 30 - 40 nm thick Ta liner at elevated temperature.

6. Deposit Cu film

7. Chemo-mechanically polish to planarize Cu and polyimide.

8. Remove nitride cap by ion etching.

9. Repeat steps 1 - 8 to build multiple levels.

Figure 1-3. Simplified schematic of a high density interconnect damascene manufacturing sequence.

8

the field metal is removed, leaving the planarized wiring and via embedded in the insulator.[7] The Si$_3$N$_4$ cap is deposited on top of the structure. Finally, for single layer structures, the nitride cap is removed by RIE. If multiple levels are built, the silicon nitride cap serves as an interlayer insulator. In this case the above steps are repeated.

1.2. Scope and Purpose of Study

The polyimides have been designed to have in-plane thermal expansion that is well matched with that of the Si substrate, to prevent the wafer from bowing during the fabrication process. One of the problems with this combination of materials, however, is the large out-of-plane CTE of the polyimide (it can be as high as 200 ppm/°C). During the manufacturing process the structure is heated to 350 - 400 °C and the out-of-plane CTE mismatch between the polyimide and the copper (CTE - 16.5 ppm/°C) will cause shear stress concentration at Cu/polyimide interfaces normal to the substrate. As a result, polyimide delamination and via deformation may occur. Different polyimides have different out-of-plane coefficients of thermal expansion and those high density interconnects fabricated with lower out-of-plane CTE polyimides should have fewer failures due to thermal stress.

Knowledge of the out-of-plane CTE of polyimides is required for design of the structures and finite element modeling of their behavior. Information about local stress distribution at interfaces, normal to the substrate, and about

9

stress relaxation mechanisms is also important for modeling the stresses during HDIC manufacturing processes. To address these questions, two sets of experiments were conducted.

1.2-1. Measurement of polyimide CTE

First, a new technique to estimate the out-of-plane coefficient of thermal expansion of thin films was developed. An Atomic Force Microscope (AFM) was used to measure the out-of-plane expansion of different polyimides in high density interconnects as a result of heating to 97 °C. The surface topography of HDICs fabricated from three different polyimides was measured initially at room temperature, then at 97 °C and again at room temperature after cooling the samples in air. The thermally induced deformation of polyimides was determined by comparing the topography of the similar areas on the samples at different temperatures. Generalized plane strain finite element models with different out-of-plane elastic constants for the polyimide were constructed to model the behavior of the structures. The out-of-plane CTE of the polyimides was estimated by comparison of the relative expansion of the polyimide obtained experimentally with the finite element analysis results.

10

1.2-2. Thermal deformation of HDIC as a result of imidization thermal cycle

During the manufacturing process the high density interconnects experience temperatures as high as 400 °C. This is why, in the second set of experiments, the deformation in a single level Cu/Ta/polyimide HDIC was studied as a result of 350 °C thermal cycle. The surface topography of the HDICs fabricated of two different polyimides was imaged using the AFM at room temperature before and after heating from room temperature to 350 °C in nitrogen. The out-of-plane deformation resulting from the thermal cycle was determined by comparing the topography of the same areas in the samples before and after the thermal treatment. Particular attention was paid to the out-of-plane deformation at the Cu/Ta and Ta/polyimide interfaces. In addition to "classical" high temperature deformation mechanisms, diffusion accommodated sliding at the Cu/Ta interface was observed. High-temperature deformation mechanisms of blanket Cu and polyimide films, as well as the deformation mechanisms unique to Cu/Ta/polyimide structures are discussed. Existing finite element models of high density interconnects do not consider heterogeneous deformation. As a first step toward developing more realistic finite element analysis of heterogeneous deformation in HDIC, a finite element model was created to simulate the thermally induced interfacial sliding observed during the experiments.

11

1.3. Chemical Structure and Properties of Polyimides

1.3-1. Properties of polyimides for microelectronic applications

Polyimides have found wide usage as films, coatings, adhesives, and matrix resins due to their excellent electrical and mechanical properties, high thermal and chemical stability, good solvent resistance, and dimensional stability. They have diverse applications in the electronics industry as flexible circuitry substrates, stress buffers, interlayer dielectrics, and passivation layers. To suit the microelectronics applications, a dielectric has to meet some requirements. The desired properties for a HDIC dielectric are:

- low dielectric constant ($\varepsilon < 3.0$);

- high thermal stability and high glass transition temperature. During the manufacturing process the interconnect system has to withstand temperatures well above 300 °C;

- good mechanical properties, especially at processing temperatures, for reliable integration with the conductor;

- good solvent resistance for building of high density and multiple level structures;

- high planarization for improved electric and mechanical properties of the interconnect structures;

- low thermal expansion coefficient to minimize the stresses during the manufacturing process.

12

By modifying the chemical structure of the polyimides, their properties can be altered for the optimal performance.[8] Improvements in polyimide properties have been sought by using trifluoromethyl or other perfluoroalkyl groups leading to lower moisture pickup, lower dielectric constant, and better solubility. Better combination of mechanical and electrical properties might be achieved by incorporating fluorinated groups into more rigid, nonplanar monomers (for low CTE). Some of the most promising new materials combine rigid 9,9'-bis(trifluoromethyl)-xanthenetetracarboxylic dianhydride (6FCDA) with rigid 2,2'-bis(trifluoromethyl)benzidine (TFMB). It was considered that further improvement in polyimide properties could be achieved by replacing the trifluoromethyl groups in TFMB with trifluoromethoxy substituents, which are more chemically and thermally stable. Therefore, bis(trifluoromehoxy)benzidine (TFMOB) have been used with different stiff dianhydrides, such as PMDA (pyromellitic dianhydride). As a result, fluorinated polyimides with nearly rodlike backbone structure were obtained. Strong in-plane orientation of the polyimide chains leads to highly anisotropic mechanical and electrical properties.

13
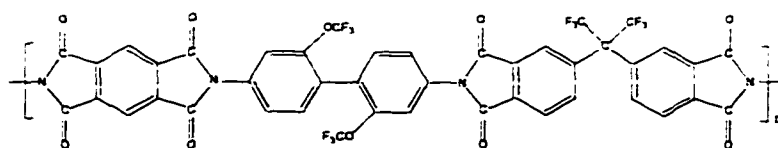
FPI-136 (PMDA-6FDA-TFMOB)
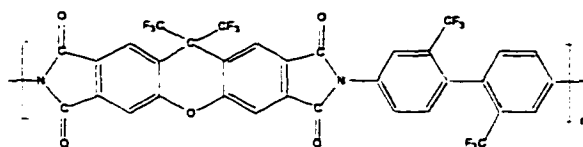
FPI-135 (6FCDA-TFMB)
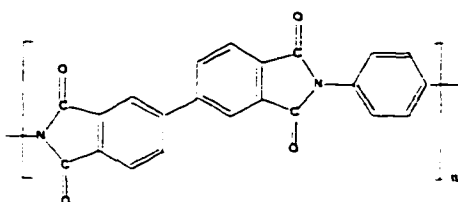
BPDA-PDA

Figure 1-4. Chemical structures of selected polyimides

1.3-2. Properties of studied polyimides

The polyimide materials used in our studies are BPDA-PDA, 6FCDA-TFMB (FPI-135) and PMDA-6FDA-TFMOB‡ (FPI-136). Their chemical structures are shown in Figure 1-4. Table 1-1 and Table 1-2 show the properties of films made with these polyimides.[8,9]

---

‡BPDA = 3,3'4,4'-biphenyl dianhydride; PDA = p-phenylenediamine; 6FCDA = 9,9'-bis(trifluoromethyl)-xanthenetetracarboxylic dianhydride; TFMB = 2,2'-bis(trifluoromethyl)-benzidine; PMDA = pyromellitic dianhydride; 6FDA = 2,2'-bis(3,4-dicarboxyphenyl)-hexafluoropropane dianhydride; TFMOB = 2,2'-bis(trifluoromethyl)xanthenetetracarboxylic dianhydride.

14

Sample	Tens. Strength, 10 % strain, MPa	Elong. Break, %	In-Plane Elastic Modulus, GPa	In-plane CTE, ppm/°C
FPI-135	200	6	6.8	7.1
FPI-136	320	10	9.8	23
BPDA-PDA	424	52	5.7	4

Table 1-1. Mechanical properties of selected polyimides

Sample	% H₂O Absorption @ 85 Rh	Dielectric Constant @ 1 MHz, dry	Thermal Stability, % thickness decrease @500 °C, 3 hrs, vacuum
FPI-135	1.3	2.5	1.4
FPI-136	1.5	2.5	1.0
BPDA-PDA	1.4	3.1	1.2

Table 1-2. Chemical, electrical and thermal properties of the considered polyimides

Film thickness of FPI-135 and BPDA-PDA polyimides is 10 μm, and FPI-136 - 5 μm. It should be noted that due to high in-plane molecular orientation of the above polyimides, their properties will be different for thinner films. Widely used commercial BPDA-PDA has become one of the first polyimides considered as a potential successor of SiO_2. Now, with the introduction of new polyimides with improved electrical properties, there are better candidates, but BPDA-PDA is included in the tables as a benchmark.

In the search for lower dielectric constant insulators, a tradeoff between dielectric constant and thermal stability has to be made. As can be seen from

15

the above tables, both FPI polyimides have lower dielectric constants, compared to BPDA-PDA, but their mechanical and thermal properties might become a problem for reliability of high density interconnects manufactured with these polyimides. Therefore, a thorough investigation of thermomechanical behavior of thin FPI polyimide films has to be carried out.

CHAPTER 2

EXPERIMENTAL TECHNIQUES

A number of modern experimental techniques are being used today to estimate the out-of-plane thermal expansion coefficient of thin polyimide films. Most of them include optical methods. Unfortunately, these methods must be applied to relatively thick (> 10 μm) polyimide films, or their resolution is not sufficient to detect the nanoscale out-of-plane expansion of thin films. For example, a 1 μm thick film with an out-of-plane CTE of 100 ppm/°C will expand out-of-plane only 10 nm on heating to 100 °C. Typical resolution of the optical methods is usually not sufficient to resolve these changes in topography. A brief summary of the most often used experimental methods is given below. Atomic force microscopy is probably the only experimental technique that is capable of resolving the angstrom-scale out-of-plane deformations.

2.1. Laser Spot Scanning Interferometry

S.T. Chen and H.H. Wagner from IBM have used a laser spot scanning interferometry[5] (LASSI) to measure the out-of-plane coefficient of thermal expansion of BPDA-PDA polyimide film between 20 °C and 400 °C.

LASSI is a sensitive instrument for measuring the small step height change during thermal cycling of the order of 1 nm in resolution. The He-Ne laser beam is split into two parallel beams when passing through a prism beam splitter. The diameter of the laser beams on the sample surface is ~20 μm. These two beams can scan across the edge of a polyimide film when the glass plate scanner rotates. At the beginning of scan, both beams are placed on the polyimide surface, but during the scanning process one beam moves across the polyimide edge first and hits the substrate surface while the other beam stays on the polyimide film surface. The two reflected beams are recombined and the interference intensity is measured to determine the phase difference between the two beams during the scanning. When the temperature rises, the polyimide expansion in the out-of-plane direction changes the laser beam phase shift. This phase shift is measured and converted into a step height change. The out-of-plane CTE can be calculated from the slope of the step height vs. temperature curve. The difference in intensity of the two different beams and the change in reflectivity of the polyimide surface during the thermal cycle are eliminated by conducting three independent measurements with a $2\pi/3$ laser phase difference. The recombined laser interference beams are directed to the photodiode mounted on a data acquisition board of a PC. This method was applied to determine the out-of-plane CTE of 21.7 μm thick BPDA-PDA polyimide film. The LASSI technique was shown to work very well for relatively thick polyimide films, and it can probably be used as well

18

for 1 μm thick films. However, the fact that the lateral resolution of this method is only around 20 μm, makes LASSI too coarse for microelectronic applications, where most of the features are under 1 μm in size, and where the submicron lateral resolution is required.

2.2. Pressure-Volume-Temperature Apparatus

Another creative method[10] to estimate elastic and thermal properties (including the out-of-plane CTE) of ~10 μm thick polyimide films was developed by Farris *et al.* In this method, they utilized Pressure-Volume-Temperature (PVT)[11] apparatus to measure the change in volume of the samples as a function of temperature and pressure. A polyimide film sample is cut in stripes, which are wrapped tightly and stuffed inside the sample cell. Then the empty space in the cell is filled with mercury, which leads to hydrostatic state of stress in the polyimide sample when the temperature in the cell is changed. The PVT apparatus then determines specific volumes from the combined volume changes of the sample and the confining mercury. It is capable of measuring specific volume changes of polymers with an accuracy of 0.001-0.002 cm^3/g.[11] For the isobaric test, the derivative of the bulk compressibility with respect to temperature is equal to the volumetric thermal expansion coefficient of the film:

$$\left(\frac{1}{V_0} \frac{\partial V}{\partial T} \right)_P = \alpha_1 + \alpha_2 + \alpha_3$$

For thin polyimide films, which exhibit transversely isotropic material

19

properties, the in-plane CTE values α_1 and α_2 are equal, and are determined by thermo-mechanical analyzer. The out-of-plane CTE is calculated from the above equation.

In our numerical models discussed in following chapters, we used the in- and out-of-plane material properties of the polyimide films obtained by Farris *et al.* Therefore, a short summary of different methods utilized to estimate the remaining material constants for polyimide films is given below. For transversely isotropic material (i.e. in-plane properties do not change with direction), there are only 5 independent material constants and two coefficients of thermal expansion. Other material constants of the 10 μm thick polyimide films are obtained using the following methods:

- *Vibrational holographic interferometry* was used to measure the in-plane Poisson's ratio. After the polyimide is cured on a substrate, it is glued to a washer, and then taken off the substrate. This allows preserving the state of stress in the film. The technique is based on a solution of the wave equation for a vibrating membrane and described in the literature.[12] It allows one to determine the residual stress in the film. After the two-dimensional state of stress σ^{2D} in the film is found a narrow ribbon is cut out of the sample. Applying the same technique to the ribbon sample allows determining a one-dimensional state of stress σ^{1D}. The in-plane

20

Poisson's ratio is then found from the following formula:

$$v_{12} = \frac{\left(\sigma^{2D} - \sigma^{1D}\right)}{\sigma^{2D}}$$

Here σ^{2D} is the in-plane principal stress for a two-dimensionally (2D) constrained film, and σ^{1D} is the stress in the same direction for a one-dimensionally (1D) constrained sample. Spin-coated polyimide films exhibit isotropic properties in plane of the film, therefore after the deposition the film is in a state of equibiaxial stress, and the two in-plane principal stresses and both in-plane Poisson's ratios are equal.

- *Tensile tests* were carried out on the samples cut in the in-plane principal direction to obtain the in-plane elastic modulus E_{11}. The in-plane shear modulus can also be found using the following relation:

$$G_{12} = \frac{E_{11}}{2(1-v_{12})}$$

- *High-pressure gas dilatometer* was used to obtain the out-of-plane Poisson's ratio v_{13}. A thin ribbon sample is strained uniaxially, pressurized with a high-pressure gas, and the stress is then measured at different pressures. The slope of stress vs. pressure plot gives a term depending on an in-plane and an out-of-plane Poisson's ratios:

$$\left(\frac{\partial \sigma}{\partial P}\right)_{\varepsilon_{11}} = 1 - v_{12} - v_{13}$$

Since v_{12} is already known, the value of v_{13} can be found.

21

- *The PVT apparatus* was used to calculate the out-of-plane elastic modulus. The changes in the specimen volume were measured as a function of applied pressure with temperature held constant. For an isothermal test over a range of pressures the change in the sample volume becomes a function of 4 independent elastic constants, one of which – the out-of-plane elastic modulus –is unknown and therefore found.

A potential problem with this method is that the PVT device was designed to be used with molten polymers, and to give precise measurements, the sample cell of the apparatus has to be stuffed tightly with the sample material. All the voids in the cell have to be filled with the confining mercury, which can be difficult to achieve. The sample cell is 2.5 cm long and 1.4 cm in diameter, which is very big, compared to micron-scale thickness of the polyimide films. Erroneous data can also be obtained during the determination of the initial volume of the sample. Therefore an error in the measurements can be expected. Besides, the measurements were done on 10 μm thick polyimide films, and one can expect different material properties in 1 μm films.

2.3. Atomic Force Microscope

Atomic Force Microscopy (AFM) was introduced in 1986[13] by a group of scientists from IBM Zurich as an offspring of Scanning Tunneling Microscopy (STM). Since then it has become a widely used technique for surface analysis. Atomic force microscopes are used in a wide variety of disciplines, including

22
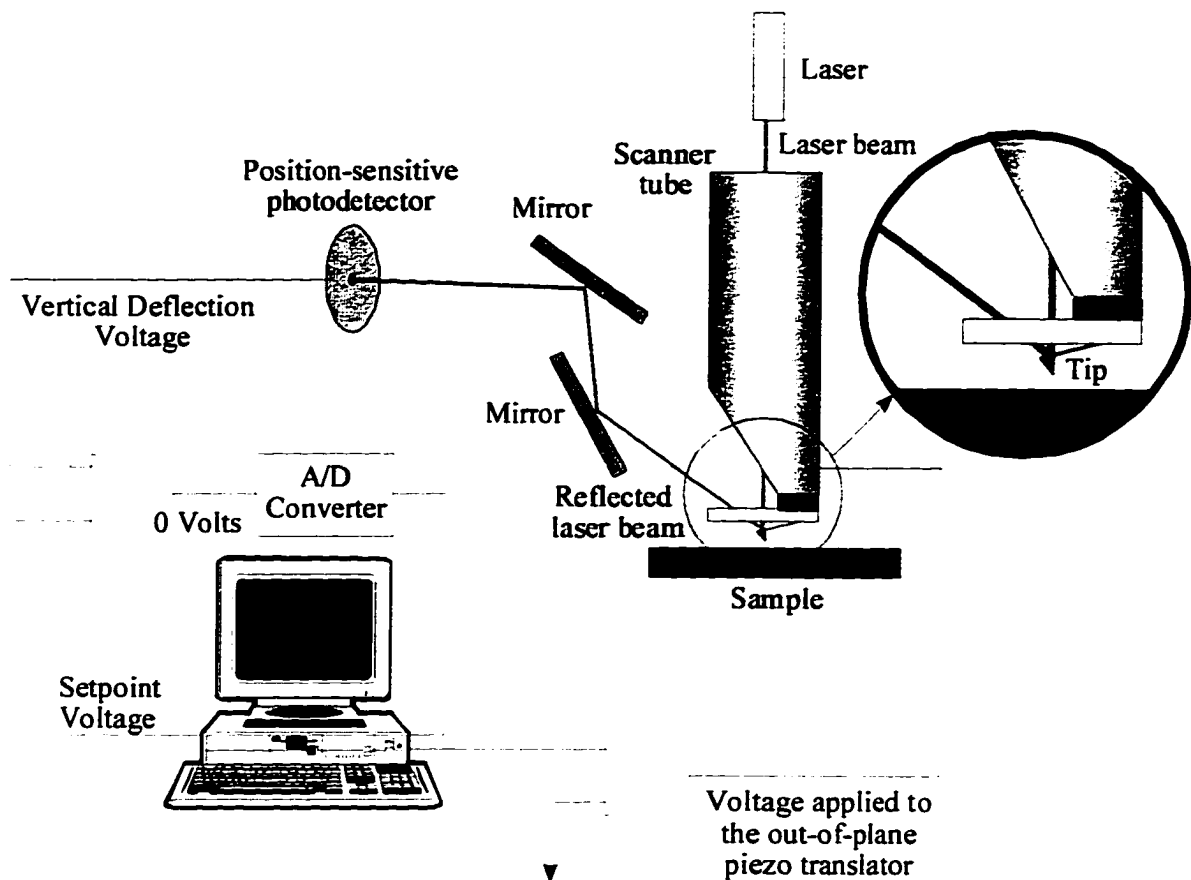
Figure 2-1. Schematic of atomic force microscope

fundamental surface analysis, and spectacular three-dimensional imaging. A schematic of a generalized AFM is given in Figure 2-1. The main components of an AFM are:

- A probe tip. The pyramidal tip is attached to the end of a 100-200 μm long cantilever. The tip is a couple of microns long, with the radius of curvature of the apex usually 5 to 40 nm.

- A 3 axis piezoelectric translator (PZT), which moves the tip over the sample in a raster pattern.

23

- A feedback system to control the vertical position of the tip.

- Deflection sensor, which measures the vertical position of the tip.

- A computer system that drives the scanner, measures data and converts it into an image.

There are three different regimes of imaging: a contact, a tapping, and a non-contact regime.

2.3-1. Contact-mode AFM

In the contact-AFM mode, an AFM tip makes soft "physical contact" with the sample. The tip is attached to the end of a cantilever with a low spring constant. The scanner gently traces the tip across the sample and the contact force between the tip and the sample causes the cantilever to bend in response to changes in topography. When the cantilever pushes the tip against the sample, the repulsive coulombic interatomic force prevents the intrusion of the tip into the sample. As a result, the cantilever deflects.

The first AFM measurements were performed by determining the cantilever deflection through detecting the tunneling current between the tip and the sample. Later other methods were developed. Now the most widely used method of cantilever deflection measurement is the method of laser beam deflection[14]. In the most common scheme shown in Figure 2-2, a laser beam bounces off the back of the cantilever onto a position-sensitive photodetector (PSPD). As the cantilever bends, the position of the laser beam on the detector shifts. Due to the short length of the cantilever, a small deflection of

24

the cantilever results in a reasonable change in angle and therefore a shift in the position of reflected laser beam. The PSPD itself can measure displacements of light as small as 10 Å. The ratio of the path length between the cantilever and the detector to the length of the cantilever itself produces the mechanical amplification. As a result, the system can detect sub-angstrom vertical movement of the cantilever tip.

Once the cantilever deflection has been detected by the AFM, the microscope can generate the topographic data set by operating in one of two modes - *constant-height* or *constant-deflection* mode.

In *constant-height mode*, the cantilever is held at the constant height as it scans over the sample surface. The voltage generated by the PSPD as a result of the laser beam deflection is used directly to generate the topographic data set. This mode can be used either on atomically smooth surfaces, where the deflections of the cantilever are small, or where the high scan speed is essential. If the constant-height mode is used on rough surfaces, this can result in significant damage to the tip or the sample.

In *constant-deflection mode*, the voltage, generated by the PSPD as a result of the laser beam deflection, is passed through the feedback loop to the piezoelectric transducer (PZT) responsible for vertical motions of the

25
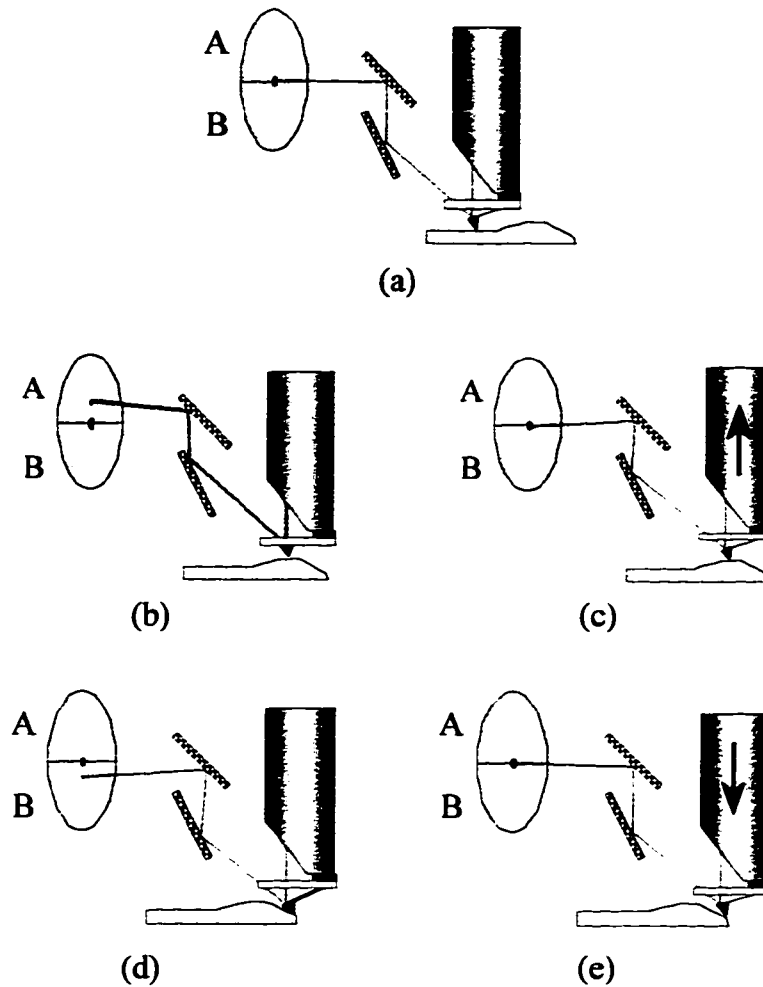
Figure 2-2. Measurement of AFM cantilever deflection by laser deflection method. Constant deflection mode of AFM.

(a) The tip scans a flat portion of the sample surface, maintaining the laser beam at the center of the position sensitive photodetector (PSPD).

(b) As the tip encounters a raised feature, the cantilever and laser beam are deflected upward onto the "A" portion of the array. With the "A" photodiode receiving an increased amount of the laser light, its voltage increases (A>B).

(c) The vertical deflection voltage difference (A-B) is sensed by the feedback electronics, causing a dropped voltage to the Z piezo crystal - the piezo retracts. As the Z piezo retracts, the tip is raised until the laser beam is recentered on the PSPD (A=B).

(d) As the tip encounters a decline in the sample topology, the tip drops. This directs more of the laser beam onto the "B" portion of the photodiode array. Voltage of the "B" portion increases (B>A).

(e) Vertical deflection voltage difference (A-B) is sensed by the feedback electronics, increasing voltage to the Z piezo crystal - the piezo extends. As the Z piezo extends, the tip is lowered until the laser beam is recentered on the photodiode array (A=B).

26

cantilever. Depending on the sign of this voltage, the PZT either expands or contracts, which moves the cantilever up or down. This restores the initial position of the laser spot in the PSPD and therefore keeps the cantilever at the constant deflection. The image is generated from the voltage applied tothe PZT to keep the cantilever at the constant deflection. This mode of AFM operation is shown in greater detail in Figure 2-2. With the cantilever deflection held constant, the total force applied to the sample is constant. The magnitude of the total force exerted on the sample varies from 10^{-7} to 10^{-6} N. In this mode the speed of scanning is limited by response time of the feedback circuit. This mode is generally preferred for most applications.

While contact AFM has been very successful for many samples, it has some serious drawbacks. The dragging motion of the probe tip, combined with adhesive forces between the tip and the surface, can cause serious damage to both sample and probe and can possibly create artifacts in the image data.

2.3-2. Tapping mode AFM

As mentioned above, even though conventional contact mode mode AFM have been used with varying success for a range of materials, it has limitations. Tapping mode was designed to overcome these limitations by placing the tip in intermittent contact with the surface to avoid dragging the tip across the surface.

27

Tapping mode imaging is implemented in ambient air by oscillating the cantilever assembly at or near the cantilever's resonant frequency using a piezoelectric crystal. The PZT motion causes the cantilever to oscillate with high amplitude (which is typically greater than 20 nm) when the tip is not in contact with the surface. The oscillating tip is then moved toward the surface until it begins to lightly touch, or "tap", the surface. During scanning, the vertically oscillating tip alternately contacts the surface and lifts off, generally at a frequency of 50,000 to 500,000 cycles per second. As the oscillating cantilever begins to intermittently contact the surface, the amplitude of the cantilever oscillation is reduced due to the tip contacting the surface. The reduction in oscillation amplitude is used to identify and measure the surface features.

During the tapping mode operation, the cantilever oscillation is maintained at constant amplitude by the feedback loop. When the tip passes over a bump in the surface, the cantilever has less room to oscillate and the amplitude of oscillation decreases. Conversely, when the tip passes over a depression, the cantilever has more room to oscillate and the amplitude increases (approaching the maximum free air amplitude). The oscillation amplitude of the tip is measured by the detector and is input to controller electronics. The digital feedback loop then adjusts the tip-sample separation to maintain constant amplitude and force on the sample.

28

Tapping mode inherently prevents the tip from sticking to the surface and causing damage during scanning. Unlike contact and non-contact modes, when the tip contacts the surface, it has sufficient oscillation amplitude to overcome the tip-sample adhesion forces. Also, the surface material is not pulled sideways by shear forces since the applied force is always vertical.

2.3-3. Non-contact AFM

Non-contact AFM is another technique in which the cantilever is vibrated near the surface of a sample. The spacing between the tip and the sample for non-contact regime is on the order of tens to hundreds of angstroms. This regime provides a means for measuring sample topography with little or no contact between the tip and the sample.

The total force between the tip and the sample in the non-contact AFM is very low, generally about 10^{-12} N. Although it can be advantageous for studying soft or elastic samples, this force is more difficult to measure compared to the force in contact regime, which is usually several orders of magnitude greater. To detect the small forces between the tip and the sample, the tip must be given a small oscillation so that AC detection methods can be used. The attractive forces extend only a small distance from the surface, whereas the adsorbed gas layer may occupy a large fraction of their useful range. Therefore, cantilevers used for non-contact mode AFM

29

must be stiffer than those used for contact AFM measurements because soft cantilevers can be pulled into contact with the sample surface. Hence, even when the sample-tip separation is successfully maintained, non-contact mode provides substantially lower resolution than contact mode.

In practice, the probe is frequently drawn to the sample surface by the adsorbed gases' surface tension, resulting in unusable data and sample damage similar to that caused by the contact technique. In addition, non-contact mode is generally impractical for routine scanning in fluids because the attractive forces are now even smaller.

2.3-4. AFM Probes

Cantilevers and their tips are critical components of an AFM system because they determine the force applied to the sample and the ultimate lateral resolution of the system. Scanning electron microscope images of different types of AFM cantilevers are shown in Figure 2-3. Integrated tip and cantilever assemblies are usually batch fabricated from silicon or silicon nitride (Si_3N_4) using photolitographic techniques. V-shaped cantilevers are the most popular, providing low mechanical resistance to vertical deflection, and high resistance to lateral torsion. These cantilevers are often used for contact-mode AFM. Rectangular cantilevers are usually used for tapping mode AFM. Cantilevers typically range from 100 to 200 μm in length, 10 to 40 μm in width, and 0.3 to 2 μm in thickness.

30
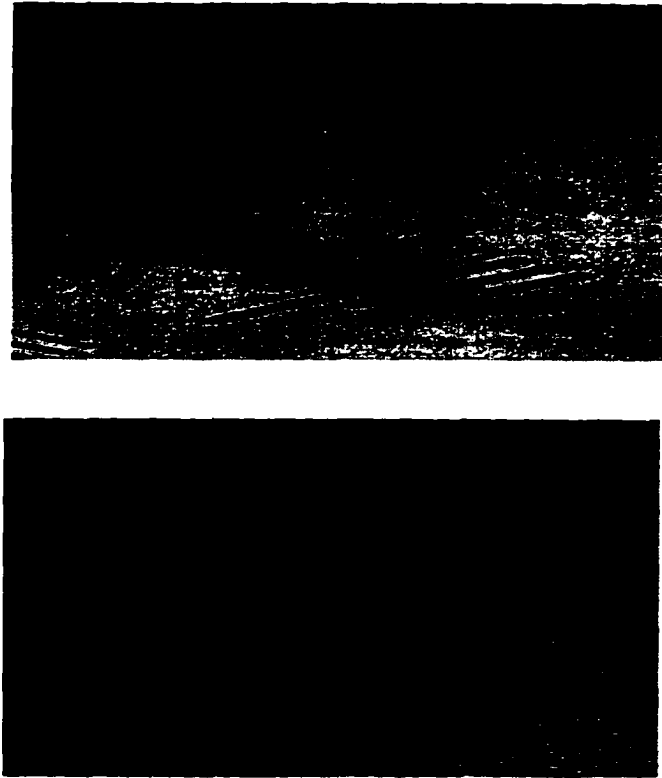
Figure 2-3. Examples of AFM cantilevers

The lateral resolution of an AFM is mostly determined by two factors: the step size of the image (equally spaced intervals at which the image data are sampled), and the sharpness of the tip. The radius of curvature of the apex of the most AFM tips ranges from 10 to 50 nm. The sharpest tips available commercially can have the radius of as small as 5 nm.

Although scanning probe microscope images are among the easiest to interpret of the images generated by any microscopy technique, they are subject to artifacts of their own. Fortunately, these artifacts are relatively easy to identify.[15]

31

- One obvious surface limitation - *deep fissures* - is represented in Figure 2-4(a). In this case, the tip is either too short or thick to reach the bottom of the recess. Although the edges would be imaged here, each square recess would be misrepresented as a wedged trench. One way around this problem is to use long, higher aspect ratio tips.

- Two similar surface limitations are represented in Figure 2-4(b): *sheer walls* and *undercuts*. In the first case, the tapering tip can not image the angles steeper than itself. Although this limitation is overcome slightly by tilting the tip, this only works in the leading edge direction. The trailing edge of the tip presents an angled aspect to the sample's wall and cannot detect any angles steeper than itself. Again, a long, higher aspect ratio tip can be used to improve image quality. Another limitation presented here is undercut features. These are voids created by overhanging material, which cannot be accessed with the tip.

- A *tilted or wedged sample* condition is represented in Figure 2-4(c). Here, the surface is tilted with respect to the tip. This introduces two possible errors: 1) elevation falsely represented as height, 2) wall angles tilted beyond the reach of tips. Therefore sample surface should be relatively parallel to the mounting plate to avoid artifacts of this type.

- Yet another related limitation is incurred when a tip becomes contaminated by debris on the sample surface. This artifact is known as a *"double tip"* condition.

32
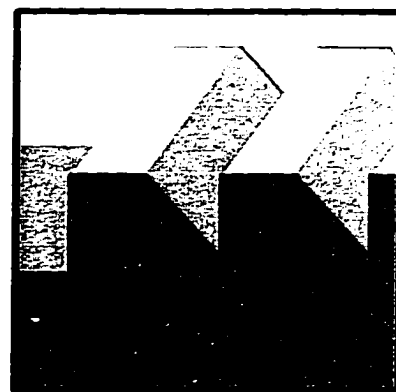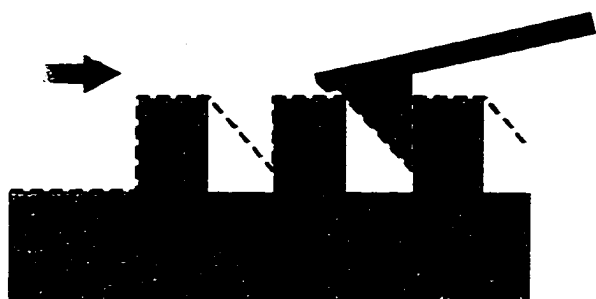
(a) Deep recesses on sample surface
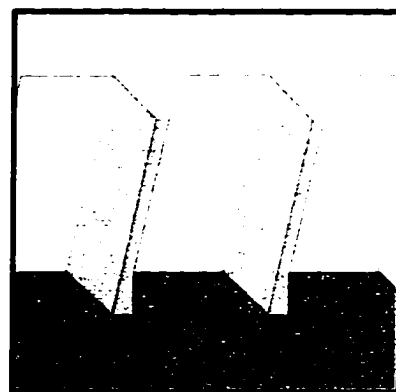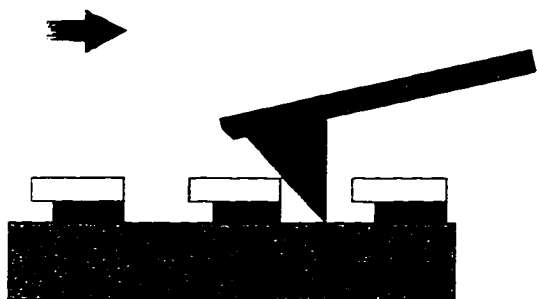
(b) Sheer walls and undercuts
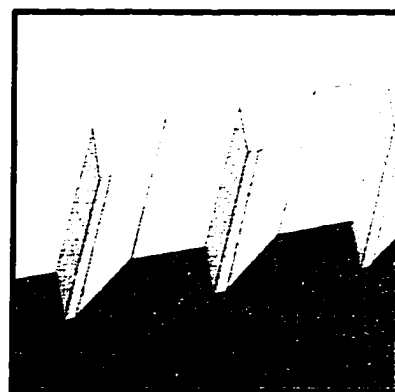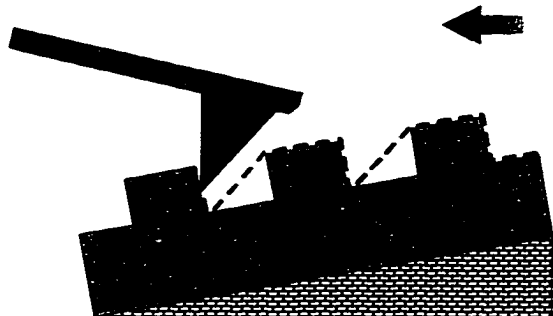
(c) Tilted or wedged sample

Figure 2-4. AFM image artifacts due to tip-sample convolution

33

Microscope	Maximum Resolution (nm)	Comments
Optical	1.8×10^2	oil immersion with 1,5000X objective
Acoustic	1.5×10	
Electron (SEM)	3-7	imaged at accelerating voltage of 1 kV
SPM (AFM)	5	limited by radius of curvature of the probe tip
Electron (TEM)	1.1×10^{-1}	imaging carbon atoms in diamond
SPM (STM)	8×10^{-2}	imaging carbon atoms in graphite

Table 2-1. Comparison of microscope resolutions[15]

2.3-5. AFM Resolution

Although atomic force microscopes can theoretically image a specimen of any size, they are practically limited by: 1) probe size; 2) scanning speed; 3) memory requirements to store electronic data; 4) the maximum travel of the scanner; and, 5) the substrate used to hold the sample. If compared to other common forms of microscopy, scanning probe microscopes (SPM) are among the microscopic techniques capable of the best resolutions (Table 2-1).

As mentioned before, the sharper tips can reveal smaller features on the surface and therefore produce better resolution AFM images. Scanning speed is also a very important parameter in the AFM resolution. The feedback loop that is used to measure the deflection of the cantilever has to have enough time to adjust the response of the out-of-plane piezoelectric translator, therefore the slower the image is acquired, the better out-of-plane resolution

34

it will have. The out-of-plane PZT range affects the maximum height of the surface features that can be resolved with the AFM. Usually, the out-of-plane PZT of an AFM has a maximum travel of about 0.005 mm. Therefore, SPMs are best suited for imaging relatively flat samples.

One of the advantages of atomic force microscopes over other existing microscope techniques is that the image is acquired as a digital three-dimensional data. Therefore, one can conduct a thorough surface analysis such as roughness, height and depth measurements of the features on the surface, grain size analysis, etc. A Digital Instruments Dimension 3000 atomic force microscope in tapping mode was used to image the areas of the samples discussed in this report.

CHAPTER 3

THERMAL EXPANSION COEFFICIENT MEASUREMENTS

3.1. Experiment Description

We developed a new technique for measuring out-of-plane thermal expansion coefficient of thin films on a substrate in this experiment. This method was applied to measure the out-of-plane expansion and to estimate the out-of-plane CTE of two 1 μm thick polyimide films. It combined an experimental technique with numerical modeling using a commercial finite element package.

Single layer HDICs manufactured by IBM with three different polyimides were used in the experiment: BPDA-PDA with an intact silicon nitride cap, and two fluorinated polyimides FPI-135 (6FCDA-TMOB) and FPI-136 (PMDA-6FDA-TFMOB), both with the Si_3N_4 cap removed. Different areas in the samples were imaged three times with the AFM: at room temperature, after heating to almost 100 °C in air, and, again, at room temperature after cooling. A special heating plate was designed for this experiment, which allowed a controlled heating and cooling of the samples in-situ, without

36
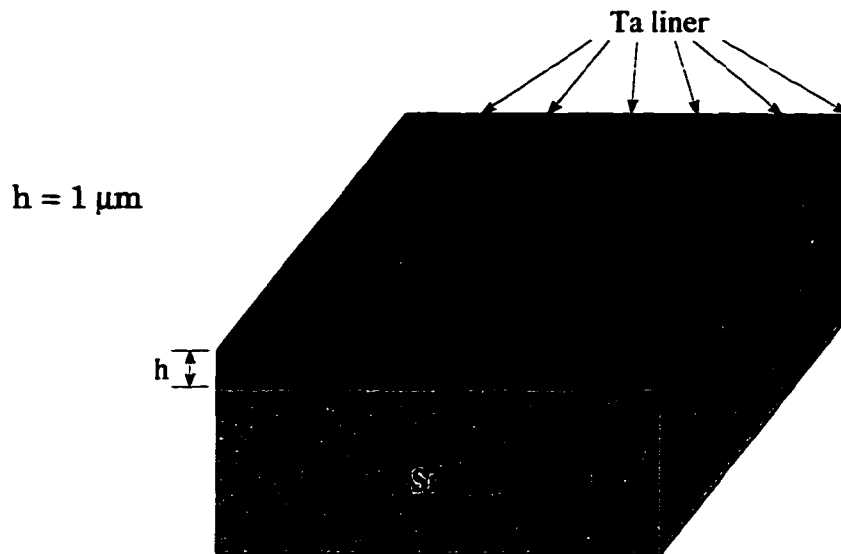
Figure 3-1. Schematic of test structure

taking the samples out of the microscope. The selection of 100 °C as a heating

temperature was not arbitrary. As mentioned above, a 1 µm thick film with

an out-of-plane CTE of 100 ppm/°C expands 10 nm out-of-plane on heating to

100 °C. This deformation is well within the resolution of the AFM. The AFM

piezoelectric material in the translator positioned above the hot sample can

potentially withstand temperatures as high as 150 °C, and during our

experiment the AFM head was cold to the touch. Therefore heating to 100 °C

yields a strong detectable signal without damaging the AFM scanner.

Several arrays of copper/polyimide line pairs were examined to determine if

there was a dependence of thermomechanical response on line width. Figure

3-1 shows the schematic of the test structures and Table 3-1 lists

Cu/polyimide line arrays that were considered during the experiment.

37

Polyimide line width (μm)	Cu line width (μm)
0.5	0.5
1	1
1.2	10
4	1
5	10

Table 3-1. Line arrays considered

The selection of parallel line arrays made it possible to use a 2-dimensional generalized plane strain finite element (FE) model to estimate the out-of-plane CTE of the polyimides. A separate mesh was constructed for each Cu/polyimide line array. Representative sections of the Cu/Ta/polyimide line arrays were modeled due to symmetry and periodicity of the structures. Boundary conditions, applied to the model are shown in Figure 3-2. Then the

$$\frac{du_y}{dz}=0 \qquad \frac{du_y}{dz}=0$$

$$u_z = 0$$
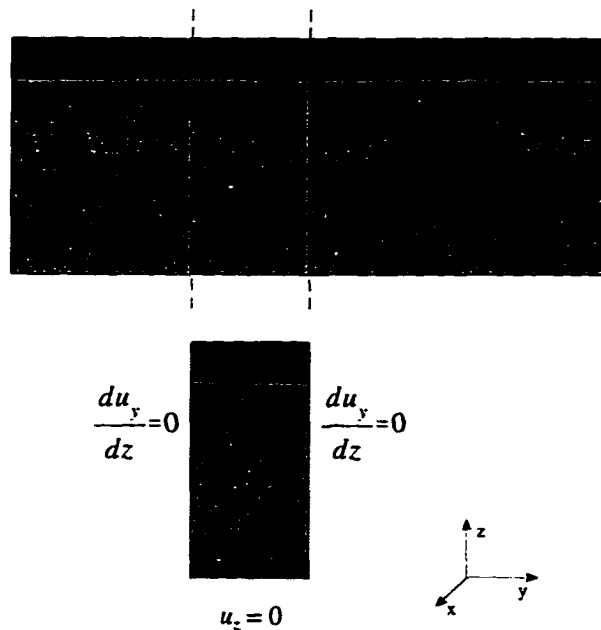
Figure 3-2. Finite element analysis setup. Due to periodicity and symmetry of the structures, a section of the line arrays was modeled

38
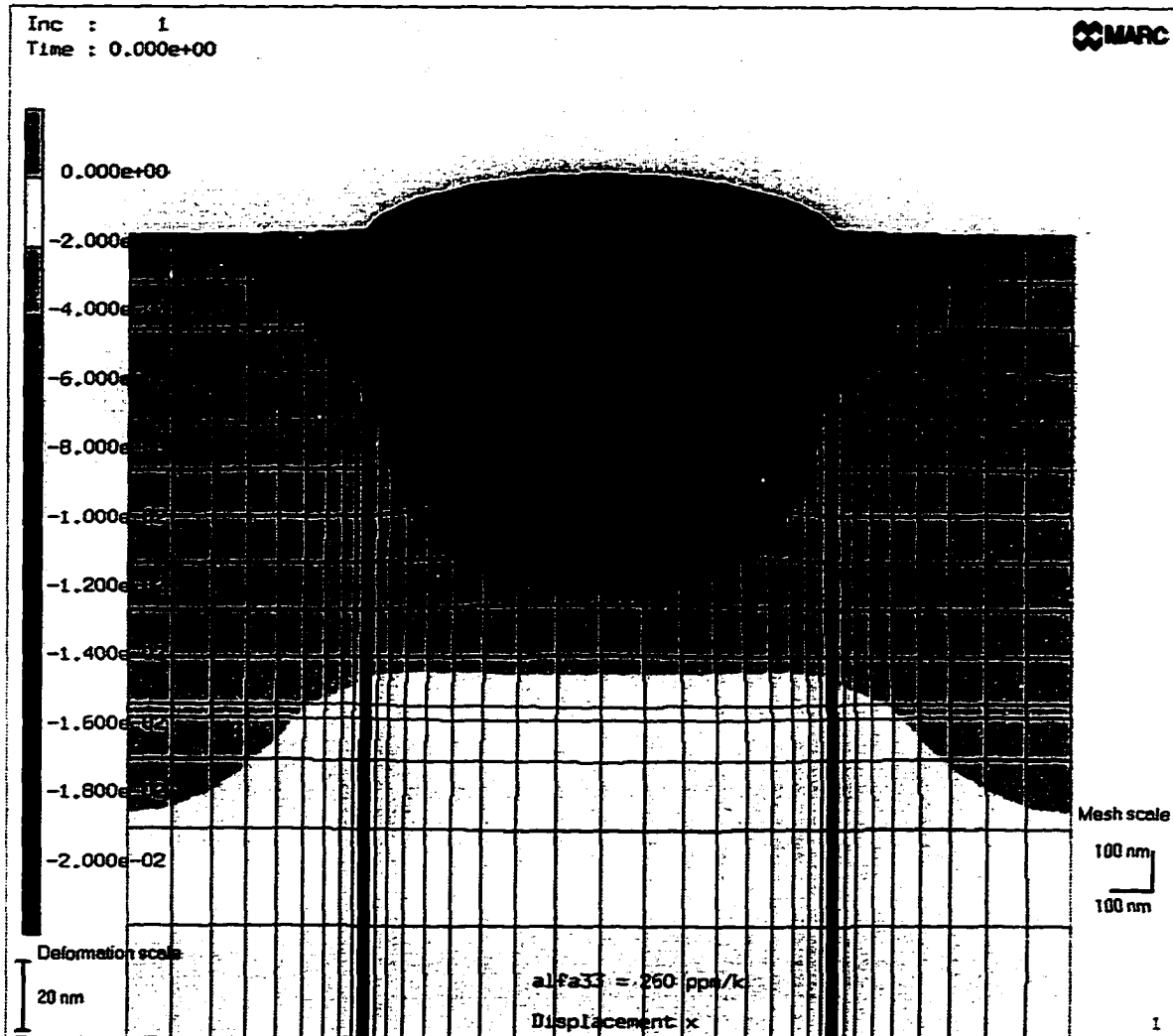
Figure 3-3. Mesh used for Finite Element analysis of 1 μm wide Cu and 1 μm wide polyimide lines. Polyimide is in the middle, it can be seen to expand out-of-plane as a result of heating to 100 °C. The expansion of polyimide is magnified 10 times for clarity.

structure was heated to 100 °C, and the relative thermal expansion of the polyimide was calculated. An example of the deformed FEA mesh showing a 3 nm polyimide expansion is given in Figure 3-3. The relative out-of-plane deformation of the polyimides predicted by the model was compared to the deformation observed during the experiments. The simulated FE experiment

39

Material	Elastic modulus, E (GPa)	Poisson's Ratio, ν	CTE, α $(10^{-6}/°C)$
Cu	128	0.36	16.5
Ta	186	0.34	6.5
Si	165	0.22	2.3

Table 3-2. Elastic properties of Cu, Ta and Si.

was run with a range of different values for the out-of-plane CTE of the polyimides. Those values that produced the best visual match between the experimental and numerical results were used to estimate of the out-of-plane thermal expansion coefficient for the given polyimide. The material constants used in the finite element model for Cu, Ta and Si are listed in Table 3-2.

The polyimide films studied in the experiments have a rigid chemical backbone structure. Polymer chains in these polyimide films are highly oriented in the film plane, however, the in-plane oriented chains are randomly aligned within the film plane.[16,17] This is why the films, manufactured of rodlike polyimides, exhibit orthotropic material properties. The degree of in-plane chain orientation strongly depends on film thickness and polyimide curing parameters, such as imidization temperature and heating rate.[18] Therefore, the out-of-plane elastic properties of the films are also dependent on the film thickness and vary from film to film depending on the curing conditions. In-plane properties, on the other hand, do not depend

40

Polyimide Orientation	Elastic Modulus, E (GPa)	Poisson's Ratio, ν	Shear Modulus, G (GPa)	CTE, α (10^{-6}/°C)
in-plane	7.5	0.35	3.0	6.0
out-of-plane	4.0 – 12.0	0.1 – 0.45	1.0 – 6.0	100 - 250

Table 3-3. Elastic constants used for polyimide.

as much on the thickness of the films, and elastic constants obtained for thicker films can be used for most numerical models. The in-plane polyimide material constants shown in Table 3-3 were obtained by Sheth, Chen, and Farris.[10,19] A range of out-of-plane material constants, also shown in Table 3-3, was considered for polyimides to bracket the effect of these constants on the thermomechanical response.

It was initially proposed to etch out the Cu and to measure the thermal expansion of a 1 µm thick polyimide film relative to the Si substrate. But the problem with this approach is that the piezoelectric translator, which is the main component of the AFM scanner, has only 1% linearity. So, if one tries to image something 1 µm high, the repeatability of the AFM will be only 1% of this height, i.e. 10 nm. This is not sufficient to estimate the thermal expansion of the polyimide. However, after the chemical-mechanical polishing the HDICs are nearly planar – the step between the copper and the polyimide is about 20-50 nm. If the Cu or Ta is used as a reference surface to estimate the expansion of the polyimide, the AFM will be able to resolve 2-5 Å, and the thermomechanical response of the whole system can be studied.

41

A Digital Instruments Dimension 3000 atomic force microscope in tapping mode was used to image samples mounted on a heating block. Images were obtained in air at room temperature and at 97 °C.

3.1-1. Effect of out-of-plane properties of the polyimide films on polyimide expansion

Before the FEA results could be compared to the deformation observed experimentally, a study had to be conducted to detect the dependence of the out-of-plane thermal expansion of 1 μm thick polyimide films on the out-of-plane elastic constants. The range of out-of-plane parameters shown in Table 3-3 covers the reasonable values that a real material might have. The FE model was run with these out-of-plane material constants and the resulting out-of-plane polyimide deformations were compared to one another. Figure 3-4 shows the polyimide deformation plots obtained from the finite element model with different out-of-plane elastic constants. It can be seen from the plots that the amount of the polyimide out-of-plane expansion does not depend strongly on the values of the out-of-plane Young's and shear moduli, and Poisson's ratio, but is significantly affected by the values of the out-of-plane CTE.

42
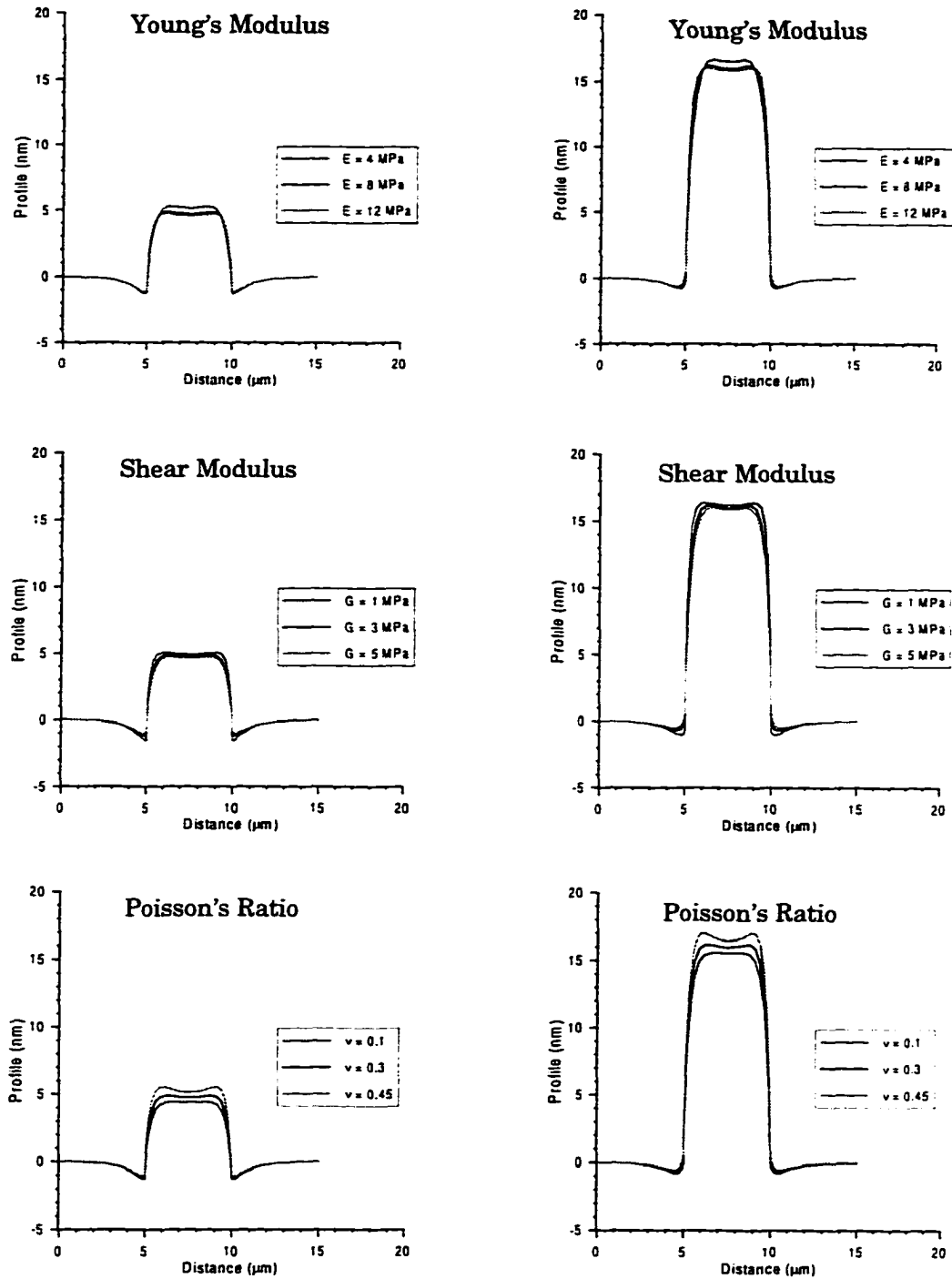
Figure 3-4. Effect of different out-of-plane material properties on thermal expansion of polyimide. Top row - Young's modulus, middle - shear modulus, bottom - Poisson's ratio. Clearly, out-of-plane CTE (α_{33}) is the most important parameter in controlling the amount of thermal expansion.

43

(a) BPDA-PDA before thermal cycle (b) The same sample at 97 °C

X: 10.0 μm/div
Z: 30.0 nm/div

(c) The sample after the thermal cycle
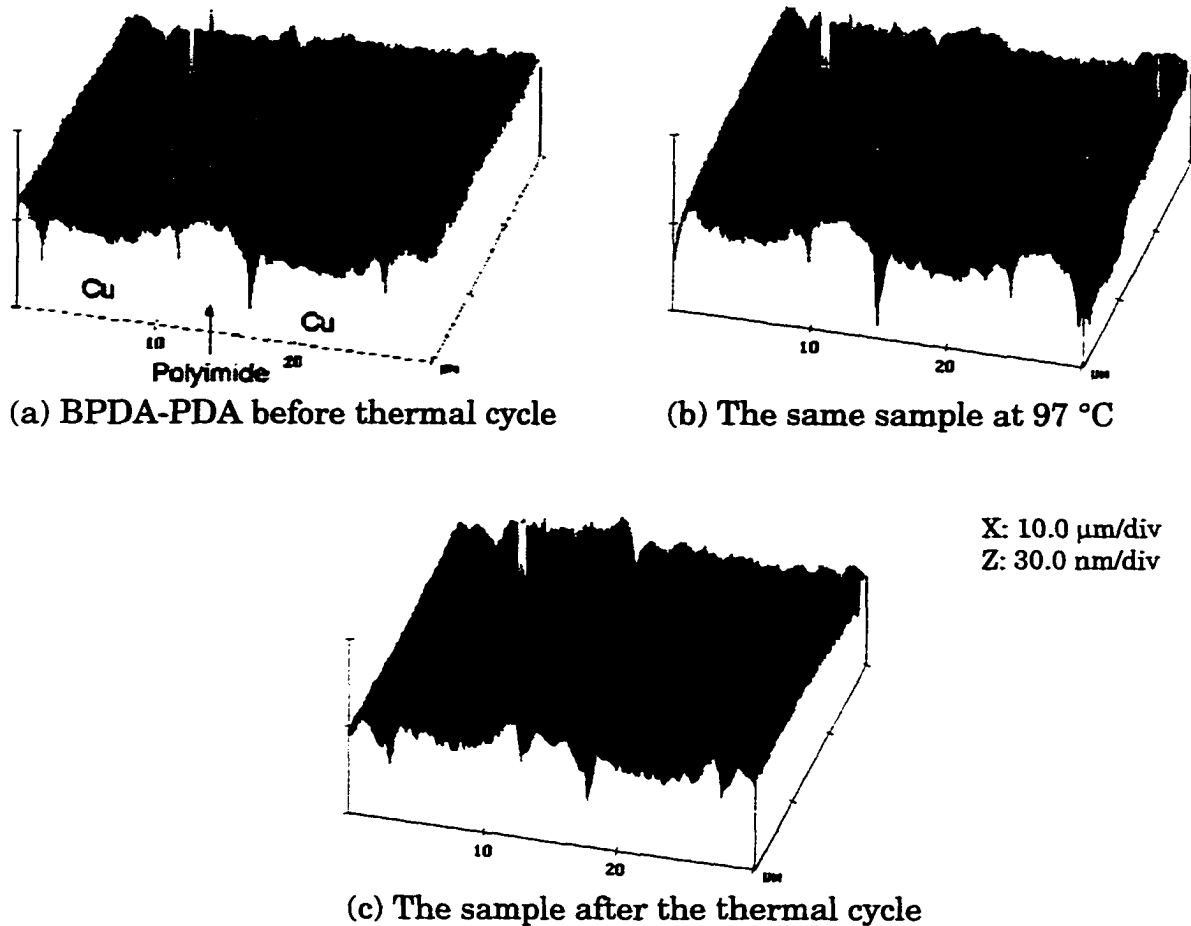
Figure 3-5. AFM images of BPDA-PDA polyimide capped with silicon nitride. 5 μm wide polyimide and 10 μm wide Cu lines. The polyimide is wavy in both room temperature images. At 97 °C the polyimide expands and the waves disappear. This behavior is attributed to buckling of the nitride cap at the room temperature due to internal compressive stress.

3.2. Results and Discussion

3.2-1. Thermal behavior of capped and non-capped polyimide

Figure 3-5 shows a 30x30 μm image of 10 μm wide Cu and 5 μm wide polyimide lines on the BPDA-PDA sample with an intact nitride cap at three different temperatures. The polyimide is wavy in both room temperature

44
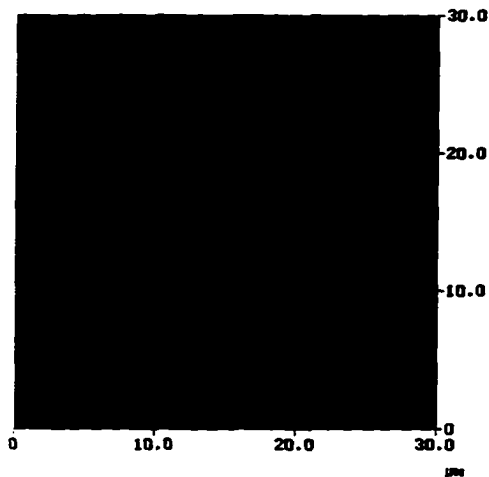
(a)   BPDA-PDA   surface
before thermal cycle
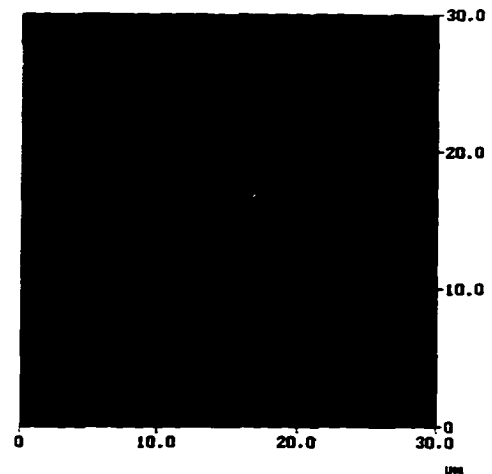
(b) Same area after heating to
97 °C

Figure 3-6. AFM images of BPDA-PDA polyimide sample capped with Si_3N_4. Note the shift in the buckles on the surface of the polyimide after the thermal cycle.

images. But, in the image obtained at 97 °C the polyimide can be seen to expand, and the waves disappear. This unexpected behavior is attributed to buckling of the nitride cap at room temperature. The nitride cap is deposited at an elevated temperature, and the CTE of the Si_3N_4 is greater than that of the polyimide. This thermal mismatch on cooling leads to formation of residual compressive stresses in the silicon nitride layer. This results in formation of 2-3 nm amplitude ripples seen on the AFM images. In other areas, as shown in Figure 3-6, the waves could be seen to shift in a more complex manner on cooling. Due to the complex behavior, the BPDA-PDA samples with intact nitride cap were not considered in the CTE studies.

45
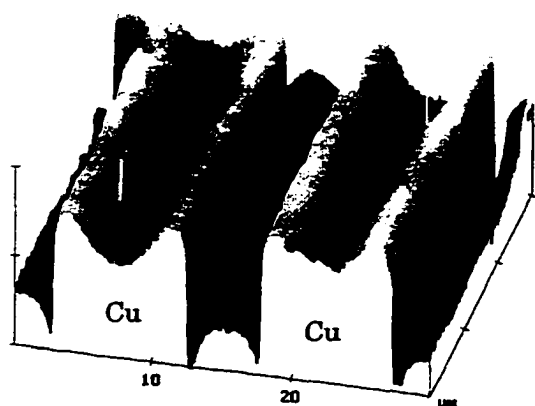
(a) FPI-135 sample before heating
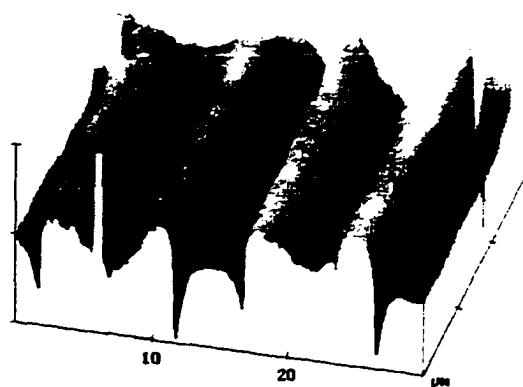
(b) The same area at 97 °C

X: 10.0 µm/div
Z: 30.0 nm/div
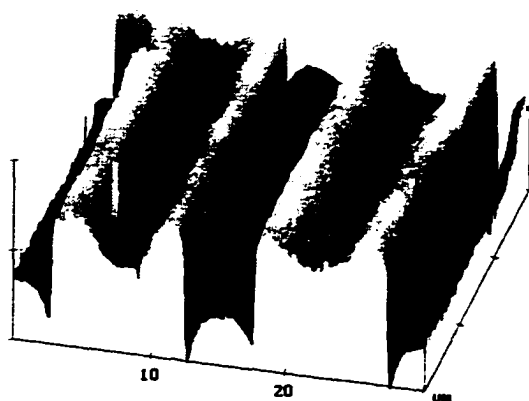
(c) The sample after the 97 °C thermal cycle

Figure 3-7. FPI-135 polyimide. 5 µm wide polyimide and 10 µm wide Cu lines. At room temperature the step between the copper and the polyimide is about 30 nm. The decrease of the relative height difference at 97 °C indicates the polyimide expansion.

Three, 30x30 µm images of 10 µm wide Cu and 5 µm wide polyimide lines taken on the FPI-135 sample are shown in Figure 3-7. At room temperature, the step between the copper and the polyimide line is about 30 nm. It can be seen that the relative height difference decreases at the elevated temperature indicating the greater expansion of the polyimide than that of the Cu.

46

3.2-2. Reference surface for the deformation plots

Since the Cu exhibits linear oxidation kinetics, it is inappropriate to use the Cu as a reference surface for measurements in air. However, the Ta in the liner exhibits logarithmic oxidation kinetics for this temperature range[20] and is, therefore, not expected to oxidize appreciably during the course of the test. So, all subtractions are referenced to the Ta liner height. The images of the surface before and after heating to 97 °C were compared to determine if the Cu oxidized appreciably. The possibility of inelastic deformation of any of the features was also evaluated by this procedure.

3.2-3. Experimental results

Cross-sectional slices through similar features and the differences between the different states for 5 μm wide FPI-135 and FPI-136 polyimide lines and 10 μm wide Cu lines are shown in Figure 3-8. The top plots represent the profiles of the same areas in the samples at room temperature before heating and at 97 °C. The bottom plots show the difference between the room temperature and the elevated temperature profiles, and represent thermal deformation of the structures as a result of heating to 97 °C. Similar profile and difference plots were obtained for all line arrays considered.

It is apparent from Figure 3-8 that the FPI-135 polyimide has much higher out-of-plane CTE than the FPI-136 (both sets of graphs have the same scale).

47

48
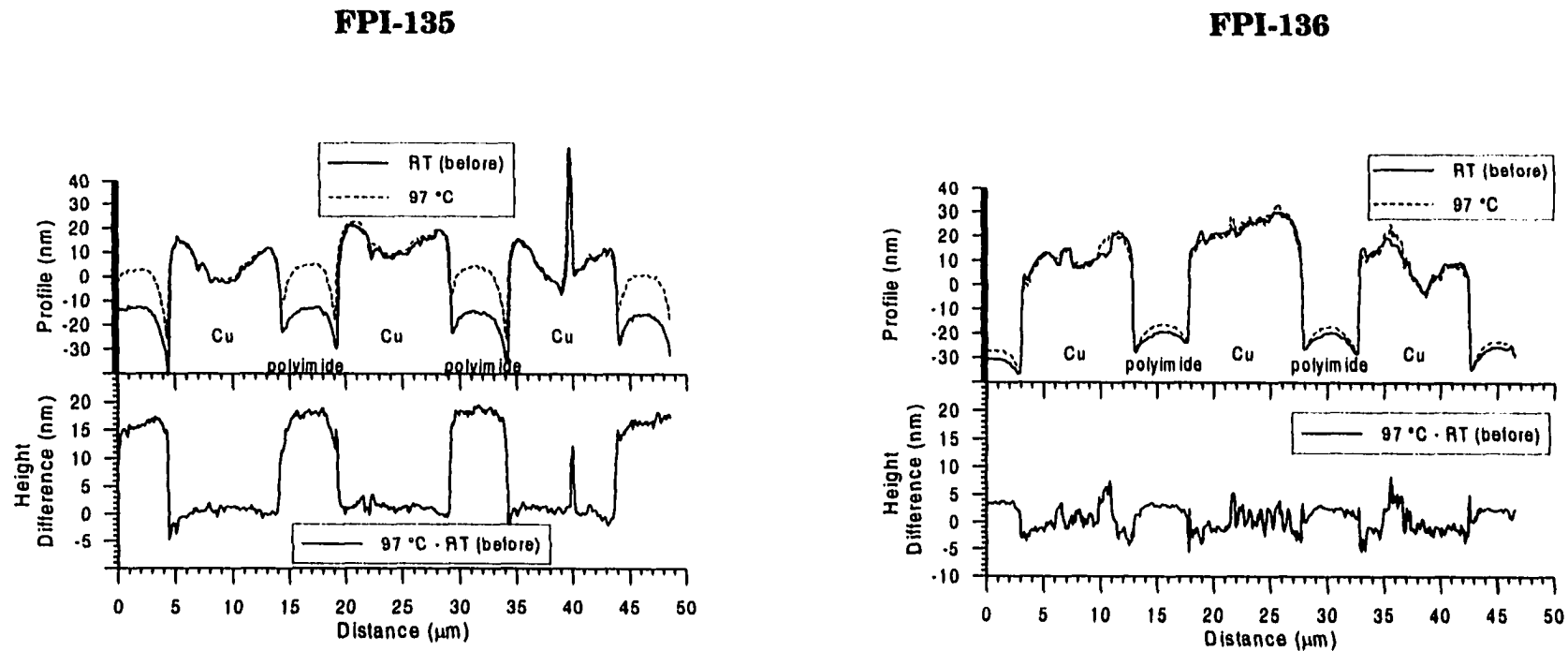
FPI-135

FPI-136

Figure 3-8. Thermal expansion of FPI-135 and FPI-136 polyimides as a result of heating to 100 °C. Top plots show sample profiles before and after heating. Bottom plots were obtained by subtraction of profiles, and they represent thermal deformation of the structures.

The narrow polyimide lines were found to exhibit atypical behavior, which will be discussed in subsequent paragraphs. For the FPI-136, all of the images comparing the initial state and the final state exhibit relative expansion of the Cu which is consistent with the oxidation of the copper.

3.2-4. Polyimide CTE estimation

Figure 3-9 compares the experimentally obtained out-of-plane deformation of the Cu-polyimide line arrays to those predictions from the finite element analysis that give the best visual match. This procedure was repeated for all line arrays considered. For the wide (5 μm, 4 μm, and 1.2 μm) FPI-135 lines, the best match between the experimental and the numerical results occurs when an out-of-plane CTE of 260 ppm/°C is used for the polyimide. The CTE of 120 ppm/°C gives the best match for the 5 μm and 4 μm wide FPI-136 polyimide lines. The oxidation of the Cu is not important, since the images were matched at the Ta/polyimide interface. The narrower polyimide lines (<1 μm for the FPI-135, and <1.2 μm for the FPI-136) exhibit significant deviation from the behavior predicted by the FE model. The numerical results obtained with the same out-of-plane CTE values overestimate the apparent expansion of both the FPI-135 and the FPI-136 polyimides in narrow lines, and it is apparent that the narrow polyimide lines are more constrained from expansion than the wider lines.

49

FPI-135

- 5 µm polyimide and 10 µm Cu lines
- 4 µm polyimide and 1 µm Cu lines
- 1.2 µm polyimide and 10 µm Cu lines
- 1 µm polyimide and 1 µm Cu lines
- 0.5 µm polyimide and 0.5 µm Cu lines

FPI-136
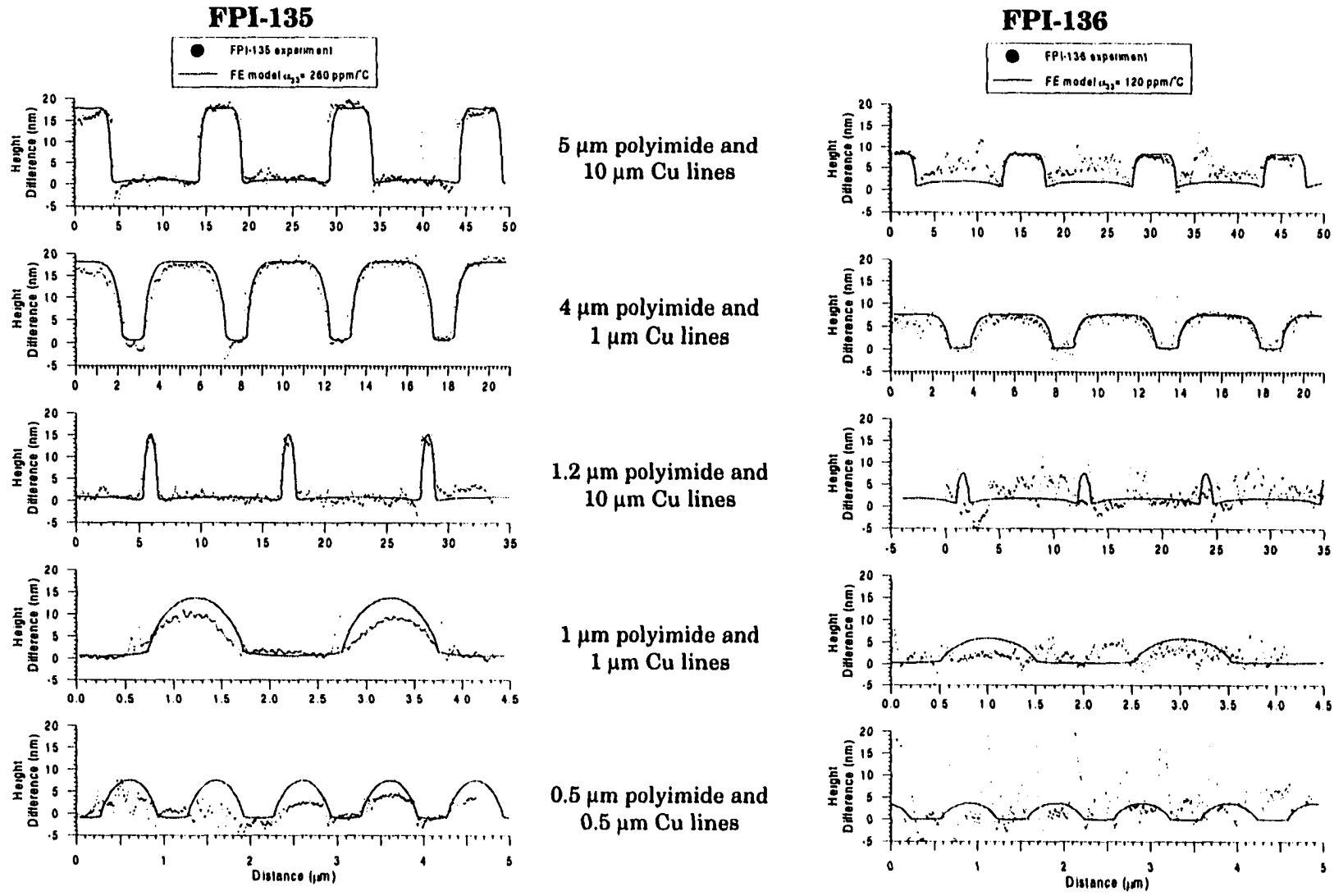
Figure 3-9. Comparison of polyimide thermal expansion predicted by FEA with experimental results

Figure 3-10. Formation of damage zone in a polyimide film as a result of reactive ion etching (RIE) step of the manufacturing process.

3.2-5. Effect of polyimide line width on thermal expansion

The increased constraint of thermal expansion for the narrow polyimide lines can be attributed to a change in properties of the polyimide at the Ta-polyimide interface as a result of the reactive ion etching (RIE). The RIE of a polyimide during the pattern generation step of the manufacturing process creates a "damage zone" at the interface. Typical polyimide chain lengths are on the order of 0.1-0.5 µm.[21] The RIE not only significantly reduces the length of the chains in the damage zone, it has also been shown[22-24] to change the chemical structure of the polyimide at the surface exposed to the high-energy ions. A schematic of this effect is shown in Figure 3-10. When the width of a polyimide line approaches the width of the damage zone, a significant change in the thermomechanical response is observed. Investigations of the thickness of the damage zone are limited by the capabilities of the apparatus, but it has been shown[22] that it can be well over 0.01 µm, and as much as 7 µm for 11 µm thick polyimide films.[23,24]

51

3.3. CTE Measurements Summary

A new method for estimation of the out-of-plane CTE of thin films was introduced. This method was utilized to measure the CTE of 1 μm thick polyimide films. For FPI-135 (6FCDA-TMOB) polyimide the out-of-plane CTE was found to be ≈ 260 ppm/°C, for FPI-136 (PMDA-6FDA-TFMOB) polyimide ≈ 120 ppm/°C.

Polyimide lines with widths equal to or less than the film thickness of 1 μm showed less thermal expansion than wider lines. This was attributed to change of polyimide properties at the Cu/polyimide interface as a result of the RIE step of the HDIC manufacturing process. When the width of the "damage zone" approaches the total polyimide line width, the thermomechanical response of the structure becomes affected by the properties of the damage zone.

Waviness observed on the surface of the BPDA-PDA polyimide was attributed to rippling of the nitride cap, which resulted from the CTE mismatch between the Si_3N_4 and the polyimide. The buckle amplitude, wavelength, and position changed on cooling. In some cases, the ripples disappeared on heating and reappeared on cooling.

CHAPTER 4

DEFORMATION AS A RESULT OF 350 °C THERMAL CYCLE

During the manufacturing of high density interconnects, the structures are subjected to temperatures well above those considered in the previous sections. The imidization temperature for most polyimides used in HDICs is 350 – 400 °C. During the fabrication of multilevel structures the first level insulator may experience as many as 10-15 cycles to the temperature of insulator curing. As was described in the previous chapter, the out-of-plane CTE of the polyimides was found to be much greater than that of the Cu. During heating the CTE mismatch creates high shear stresses at the interfaces normal to the film plane. Interfacial stresses can result in sidewall decohesion and deformation of the structures causing the failure of the device. Any attempt to quantify or model the effect of these stresses on the reliability of microelectronic devices must incorporate an understanding of the deformation mechanisms that are appropriate for the given material system. One approach used to investigate these mechanisms is to measure the development of stresses during thermal cycling of a blanket film deposited on a substrate and then try to extend the results on more complex

high density interconnect structures. Certainly, this is a valid approach, but it will not produce accurate description of deformation processes in vicinity of complex structures in HDIC, such as line arrays or vias.

The following sections report on an experimental investigation of thermomechanical deformation of copper/tantalum/polyimide line arrays in 1 μm thick high density interconnects. Stress-temperature behavior and the stress relaxation mechanisms in Cu and polyimide blanket films, as described by other researchers are also discussed. Then the experimental observation of stress-relaxation mechanisms specific to the Cu/Ta/polyimide interconnect structures is introduced.

4.1. Experiment Description

This chapter reports on the use of an atomic force microscope (AFM) to study deformation in a single level Cu/Ta/polyimide HDIC as a result of the polyimide imidization thermal cycle. The surface topography of HDICs fabricated with two different polyimides was measured at room temperature before and after heating to 350 °C in nitrogen. One HDIC was manufactured with the FPI-135 (6FCDA-TFMB) polyimide, and another was manufactured with the FPI-136 (PMDA-6FDA-TFMOB) polyimide. The samples were heated in gettered nitrogen from room temperature to 350 °C at a standard rate used in the HDIC manufacturing process - 2 °C/min. Then they were cooled down to room temperature at the same rate. A Digital Instruments

54

Dimension 3000 atomic force microscope in tapping mode was used to image the same areas of parallel line arrays in the samples in air at room temperature before and immediately after the thermal cycle. The out-of-plane deformation resulting from the thermal cycle was determined by comparing the topography of the same areas in the samples before and after the thermal treatment.

Particular attention was focused on out-of-plane deformation at the Cu/Ta and Ta/polyimide interfaces. The damascene processing of the Cu/polyimide structures yields smooth, vertical Cu/Ta/polyimide interfaces. As a response to the shear stress generated by the out-of-plane CTE mismatch between the polyimide, the Ta, and the Cu, it was expected to see diffusion-accommodated interfacial sliding at the interfaces normal to the substrate plane. Our previous results[25] showed that the out-of-plane CTE of the FPI-135 structures was almost twice that of the FPI-136 structures. So, more interfacial sliding was expected in the FPI-135 samples. Also, it was previously observed that expansion of the narrow polyimide lines was more constrained and this was attributed to a damage zone from the reactive ion etch. Therefore, less sliding at the interfaces parallel to the narrow polyimide lines was expected. For these reasons, we measured the residual deformation at the end of an imidization thermal cycle for different Cu and polyimide line widths and for the two different polyimides. The line array combinations

55
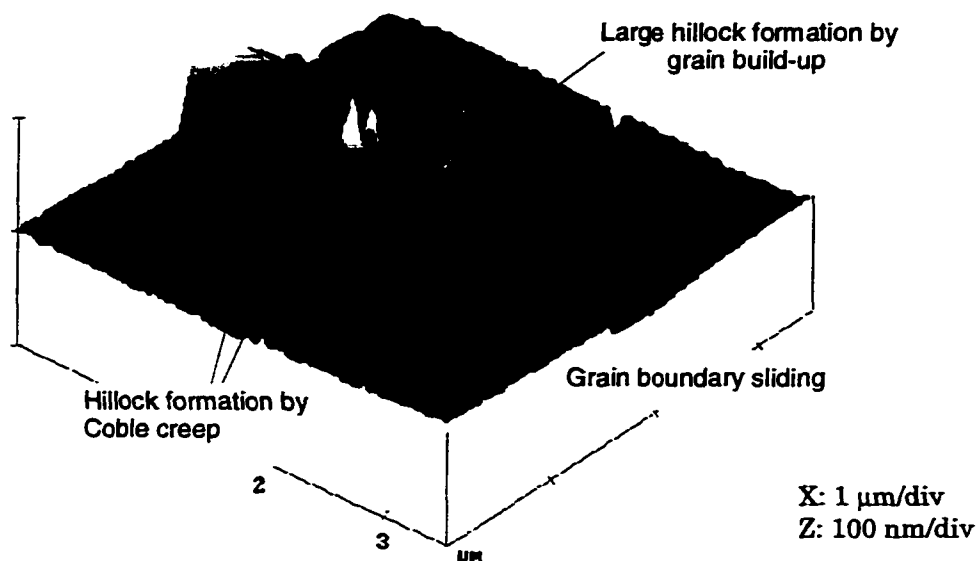
Figure 4-1. AFM image of the Cu surface after the 25 °C - 350 °C - 25 °C thermal cycle

shown in Table 3-1 on page 14 were examined to determine if there was a dependence of thermomechanical response on line width. The width of the Ta liner between the Cu and the polyimide in all cases was 20-50 nm.

4.2. Results

4.2-1. AFM observations

An AFM image of a 3.5 µm area of the Cu 2-3 µm away from the interfaces after the thermal cycle is shown in Figure 4-1. Prior to thermal cycling, the Cu surface was nearly atomically smooth with a RMS roughness on the order of 0.5 nm. The observed change in relative elevation of the grains is attributed to the response of the film to the biaxial in-plane stress. To relax the stress, the matter flows through the boundaries from the grains into

56

selected adjacent grains, which results in grain build-up at the expense of the neighbor grains.[26] The difference in grain elevation for various Cu grains can be attributed to differences in grain orientation. It has been proposed[26,27,28] that the stress gradients between <110> and <111> grains lead to large hillock formation by preferred growth of <110> grains out of the film plane. The buildup of material on the grain boundary in the left part of the image is attributed to stress relaxation by Coble creep where mass flows to the film surface by grain boundary diffusion. The grain boundary steps seen in the front right portion of the image are the result of grain boundary sliding.

As mentioned above, diffusion accommodated grain boundary sliding can cause relaxation of interfacial shear stresses. The AFM image in Figure 4-2(c) shows a deformation map of a line array structure as a result of the thermal cycle. This image was obtained by subtraction of the AFM images of the same area before and after the thermal cycle (Figure 4-2(a) and Figure 4-2(b)). Sliding at Cu/Ta/polyimide interface can be easily observed on this image, but it is not clear whether the sliding took place on Cu/Ta or Ta/polyimide interfaces. Figure 4-3 shows a close-up view of a slice through the Cu/Ta/polyimide interface before and after the thermal cycle. All the sliding occurs at the Cu/Ta interface and there is no evidence of the Ta sliding at the Ta/polyimide interface. The polyimide appears as if it is being "held up" at the Ta/polyimide interface.

57
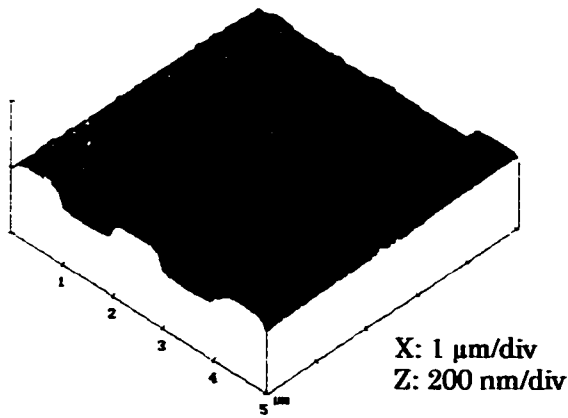
(a) Area of an FPI-135 sample
before 350 °C thermal cycle

X: 1 μm/div
Z: 200 nm/div
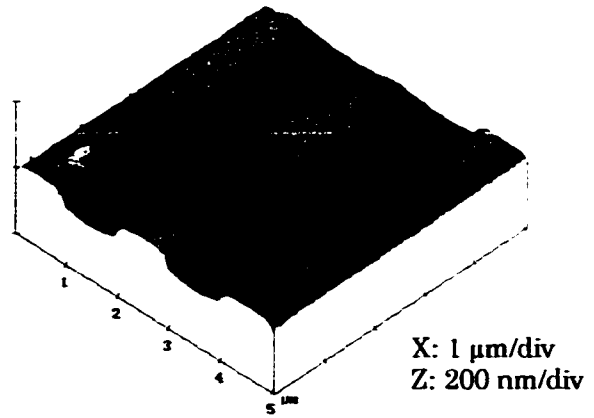
(b) The same area after the
thermal cycle

X: 1 μm/div
Z: 200 nm/div

X: 1 μm/div
Z: 100 nm/div
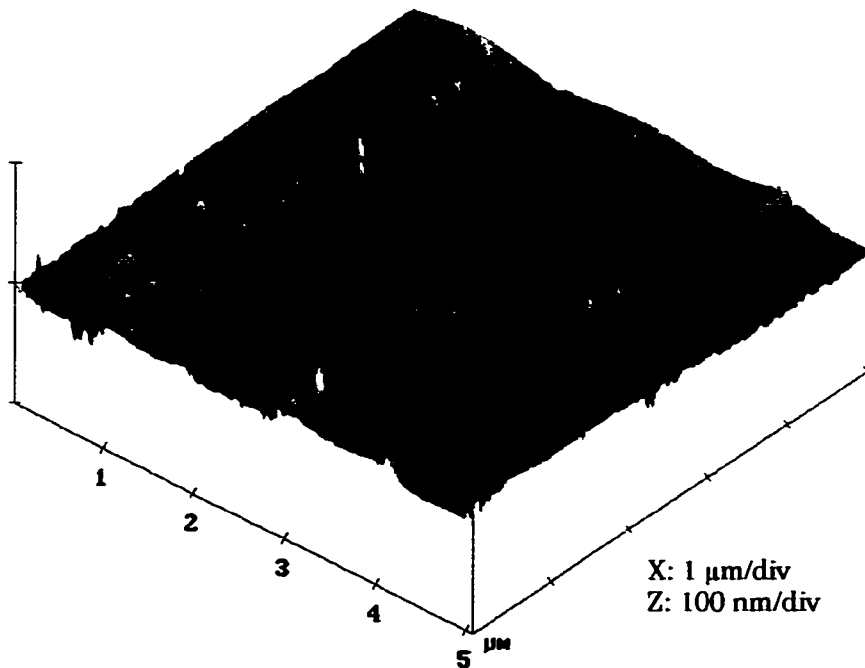
(c) Deformation as a result of the
350 °C thermal cycle

Figure 4-2. AFM images illustrating sliding at Cu/Ta/polyimide interface. Bottom image was obtained by subtraction of images (a) and (b) and it shows the deformation as a result of 25 °C – 350 °C – 25 °C thermal cycle.

58
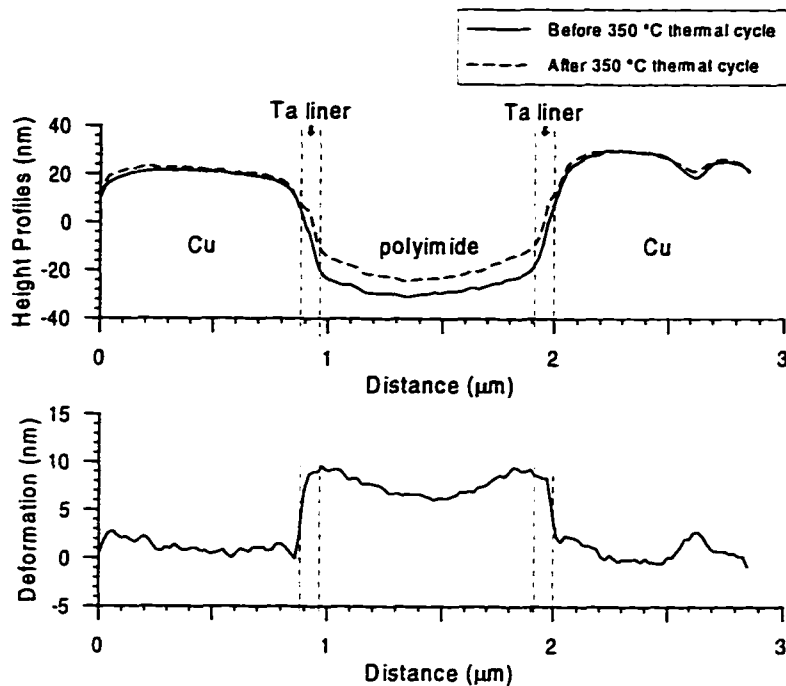
Figure 4-3. Profile and deformation plots of a Cu/Ta/polyimide interfaces. Deformation plot was obtained by subtraction of the height profiles. The step between the tantalum and the copper surfaces suggests that the sliding occurred at the Cu/Ta interface. There is no evidence of sliding at the Ta/polyimide interface.

4.2-2. FPI-135 sample

It was proposed that narrow (≤ 1 μm wide) polyimide lines would exhibit less Cu/Ta interfacial sliding because the thermal expansion was previously observed to be more constrained. Figure 4-4 shows cross-sectional slices through the same features in 4 μm /1 μm and 1 μm /1 μm wide polyimide/Cu line arrays in the FPI-135 sample. The top plots represent the room temperature profiles of the same area before and after heating to 350 °C. The bottom plots represent a difference between the "after" and "before" slices
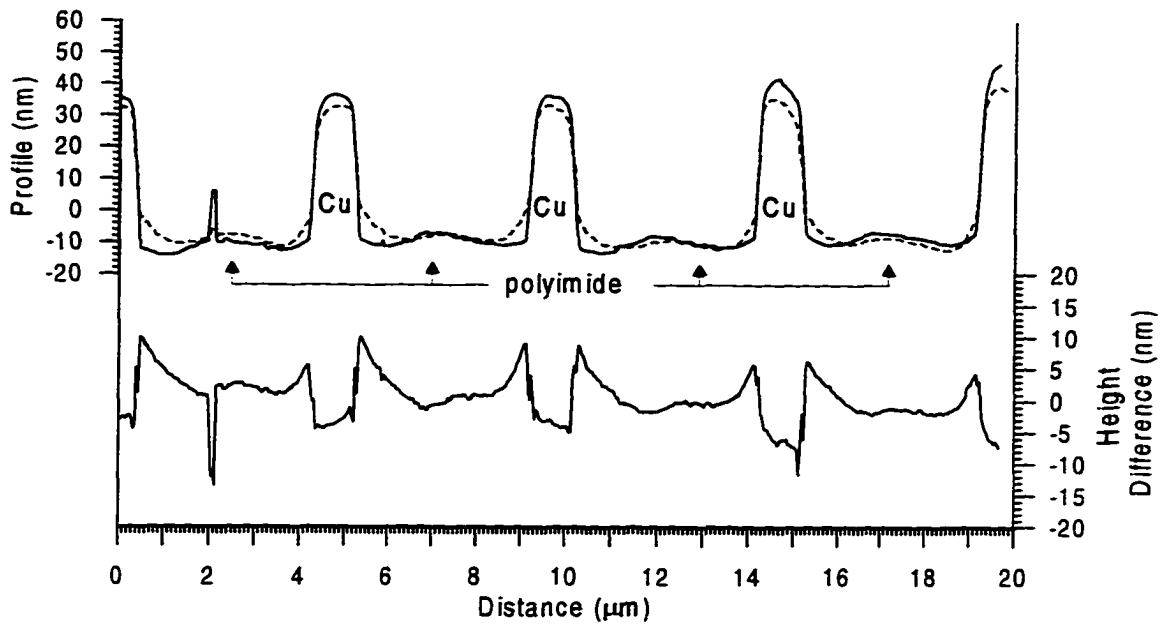
59
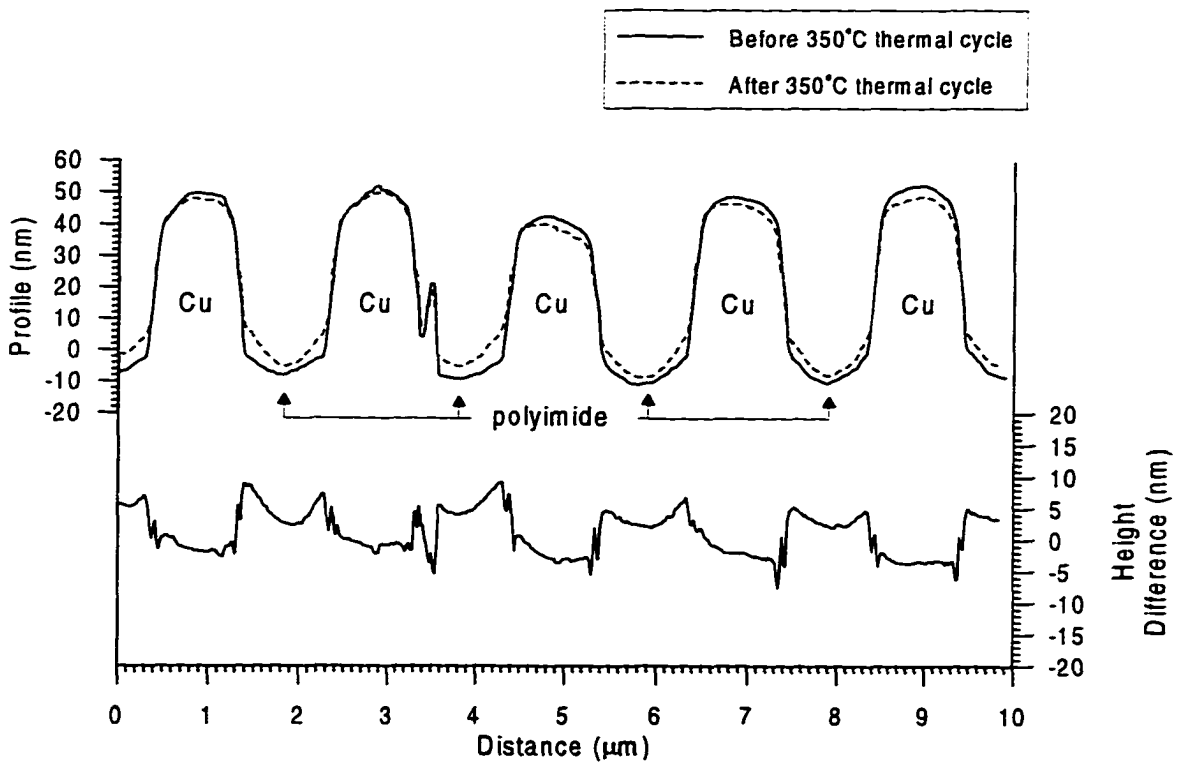
Figure 4-4. Deformation plots for 1 μm wide Cu lines in FPI-135 sample
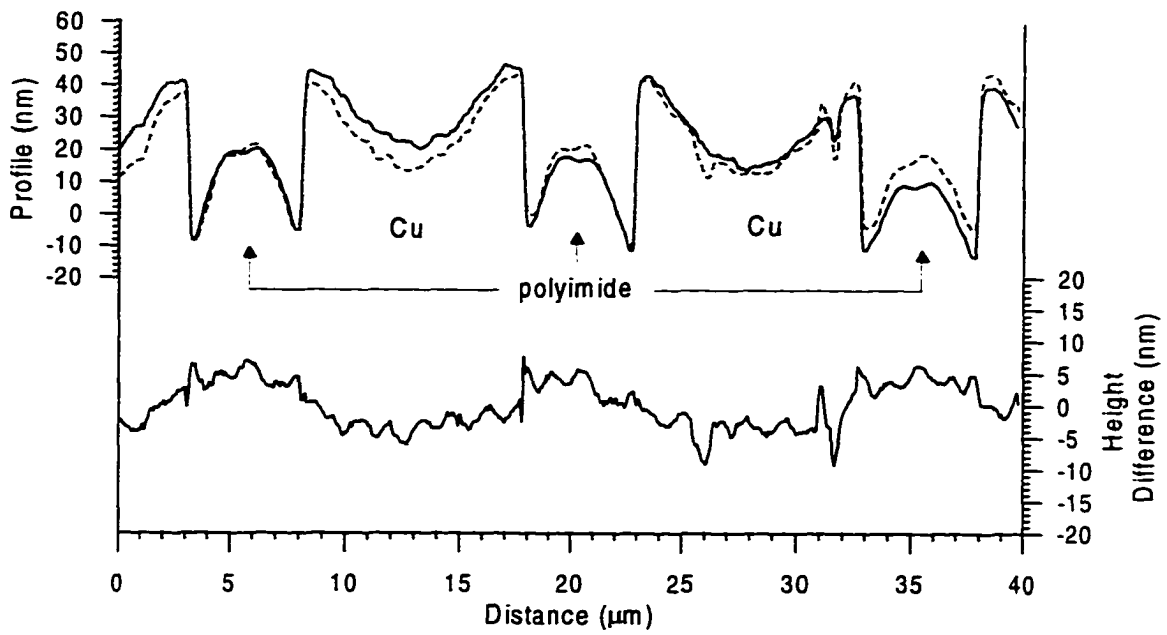
60

(a) 5 μm wide polyimide and 10 μm wide Cu lines
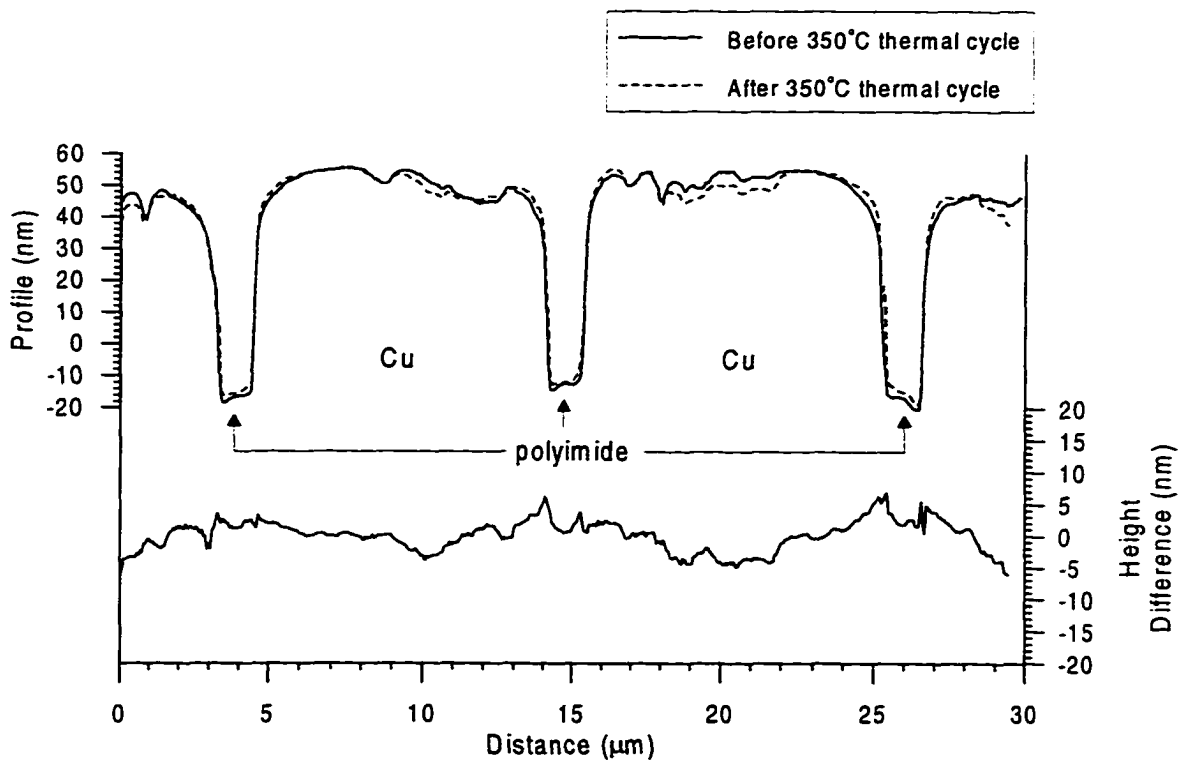
(b) 1.2 μm wide polyimide and 10 μm wide Cu lines

Figure 4-5. Deformation plots for 10 μm wide Cu lines in FPI-135 sample

61

and show the residual deformation. In the deformation (bottom) plots in both areas, the polyimide surface is curved as if it is being held up at the interface. For 4 μm wide FPI-135 lines there is a 10 - 13 nm discontinuous step at the Cu/Ta interface and for 1 μm wide polyimide lines this step is 8 -10 nm. The magnitude of the Cu/Ta sliding is decreased to 3 - 5 nm as the width of the polyimide lines is decreased to 0.5 μm. Thus our expectation that narrow polyimide lines exhibit less sliding is confirmed.

In contrast to the 1 μm wide Cu lines (Figure 4-4), little or no Cu/Ta sliding is observed for line arrays with 10 μm wide Cu lines. This can be seen in Figure 4-5 which shows the profiles and the deformation plots for 5 μm /10 μm and 1.2 μm/10 μm wide polyimide/Cu line arrays in the FPI-135 sample.

4.2-3. FPI-136 sample

The AFM images in Figure 4-6 show a 2.5 μm by 3.5 μm FPI-136 polyimide via surrounded by Cu. The first image (a) shows the surface before the thermal cycle, the second (b) shows the surface after the cycle, and the third (c) shows the difference in topography as a result of the thermal cycle. The difference in the Cu topography provides visual evidence that a Cu corrosion product was desorbed during the thermal cycle in the FPI-136 sample. No such corrosion product desorption was observed on the Cu surface on the FPI-135 sample. We previously observed growth of a corrosion product on

62
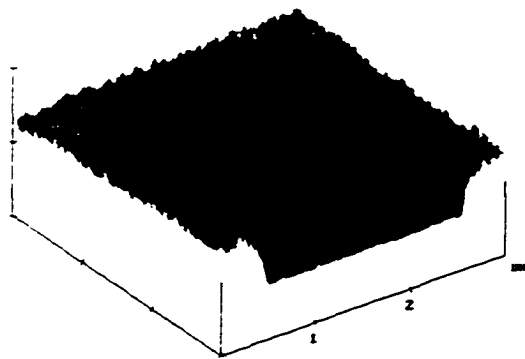
(a) Polyimide via in Cu before thermal cycle
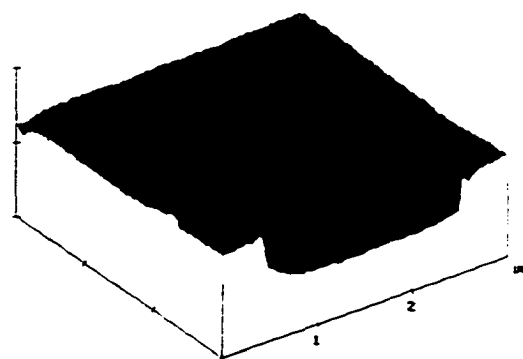
(b) The same area after thermal cycle

X: 1 μm/div
Z: 100 nm/div
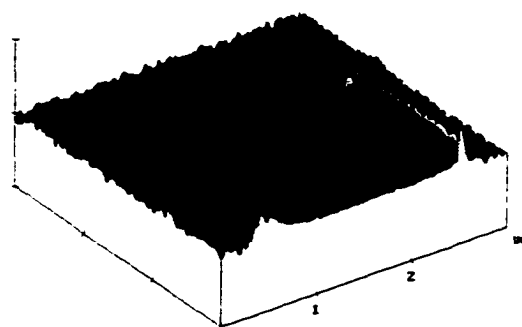
(c) Deformation as a result of thermal cycle

Figure 4-6. AFM images showing interfacial sliding and desorption of Cu corrosion product in the FPI-136 sample as a result of the 350 °C thermal cycle.

FPI-136 samples heated to 100 °C in air, while none was observed in the FPI-135 samples. The instability of the Cu surface in the FPI-136 samples can be attributed to differences in processing or age between these samples.

Figure 4-6(c), the change in surface topography as a result of thermal cycle, clearly shows that the edge of the polyimide via is being held up at the interface. However, the desorption of the corrosion product makes it difficult

63

to ascertain how much of the Cu-Ta step height change is due to Cu/Ta interfacial sliding. If we assume that the process of the Cu corrosion product desorption occurred uniformly across the sample, some comparisons can still be made. Figure 4-7 shows the deformation plots for the FPI-136 sample. In the area of 4 μm/1 μm wide polyimide/Cu lines the step is 22 - 29 nm, and for 1 μm/1 μm wide polyimide/Cu line arrays it is 19 - 26 nm. Again, the amount of Cu/Ta interfacial sliding is greater for the wider polyimide lines. Also, as for the FPI-135 sample, the magnitude of the interfacial sliding is decreased for wider Cu lines. As can be seen in Figure 4-8, in the area of 5 μm/10 μm wide polyimide/Cu lines the height of the step is 14 - 17 nm, and in the area of 1.2 μm/10 μm wide polyimide/Cu lines it is 10 - 13 nm. In contrast to the FPI-135 sample, the residual deformation of the FPI-136 polyimide shows that it is being held up at the interface for all line widths. A summary of the step heights is given in Table 4-1.

	Step height change for different line arrays (nm)				
	0.5 μm wide Cu	1 μm wide Cu		10 μm wide Cu	
Sample	0.5 μm wide polyimide	1 μm wide polyimide	4 μm wide polyimide	1.2 μm wide polyimide	5 μm wide polyimide
FPI-135	3- 5	8 - 10	10 - 13	0 - 2	2 - 5
FPI-136	10 - 15	19 - 26	22 - 29	10 - 13	14 - 17

Table 4-1. Step height change (nm) at the Cu/Ta interface. (Note that the step height change for the FPI-136 samples includes desorption of a corrosion product.)

64
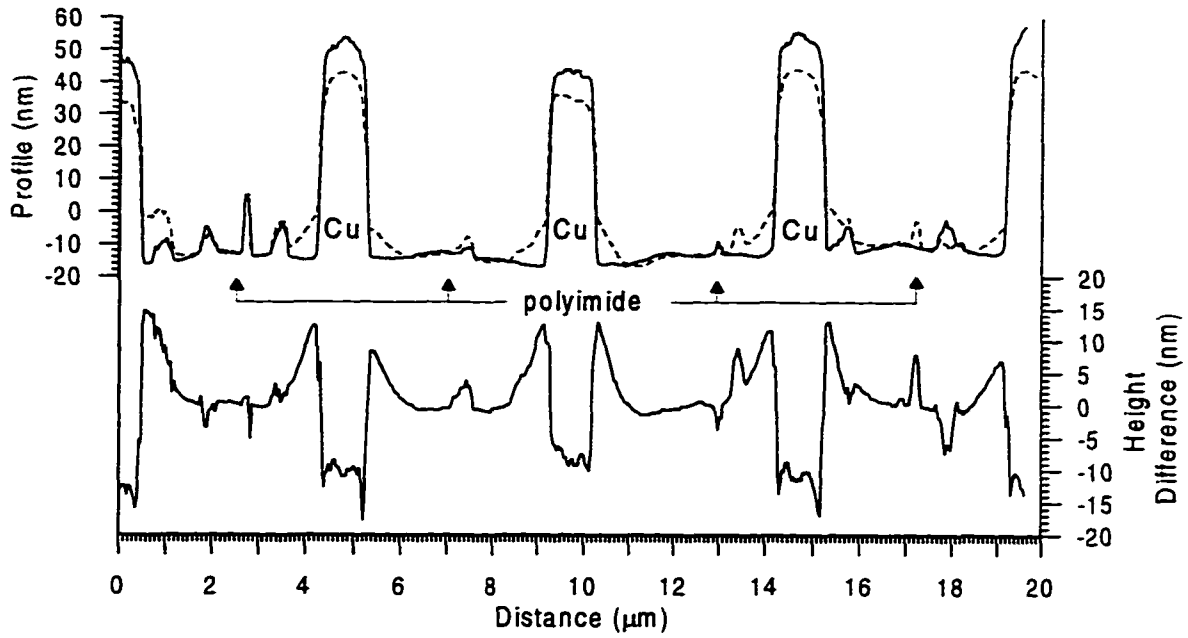
(a) 4 μm wide polyimide and 1 μm wide Cu lines
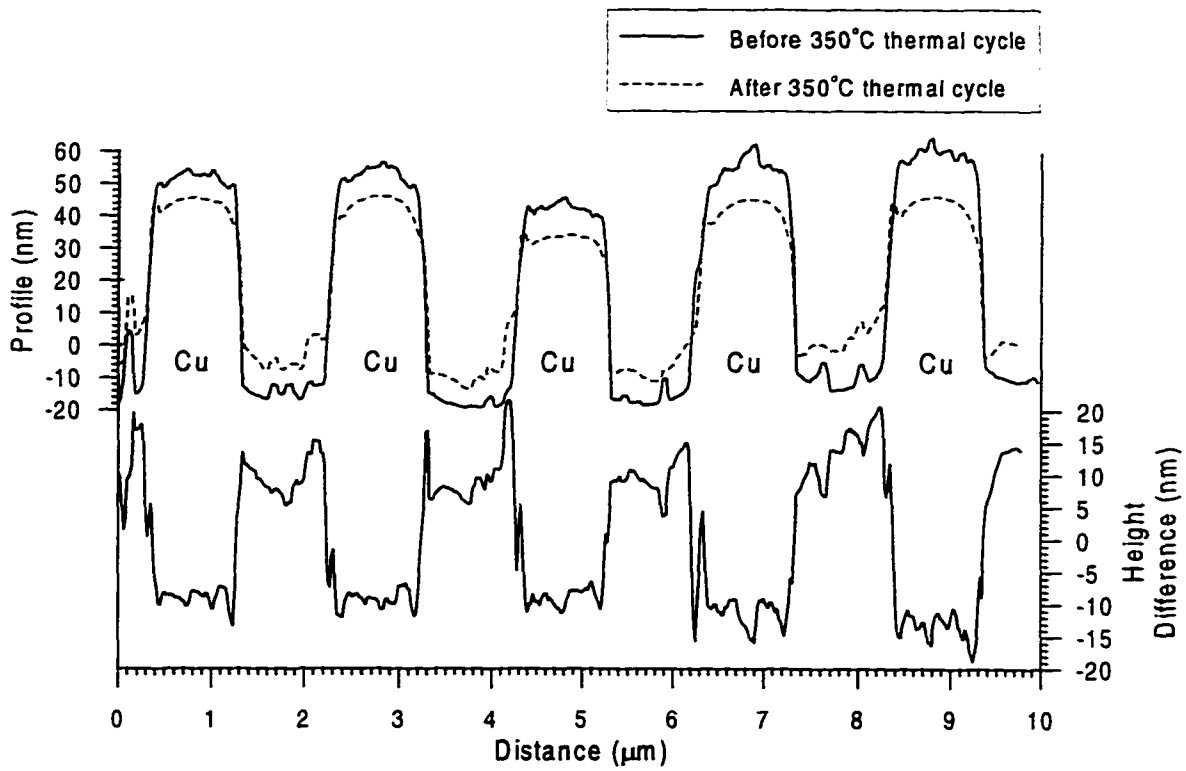
(b) 1 μm wide polyimide and 1 μm wide Cu lines

Figure 4-7. Deformation plots for 1 μm wide Cu lines in FPI-136 sample

65
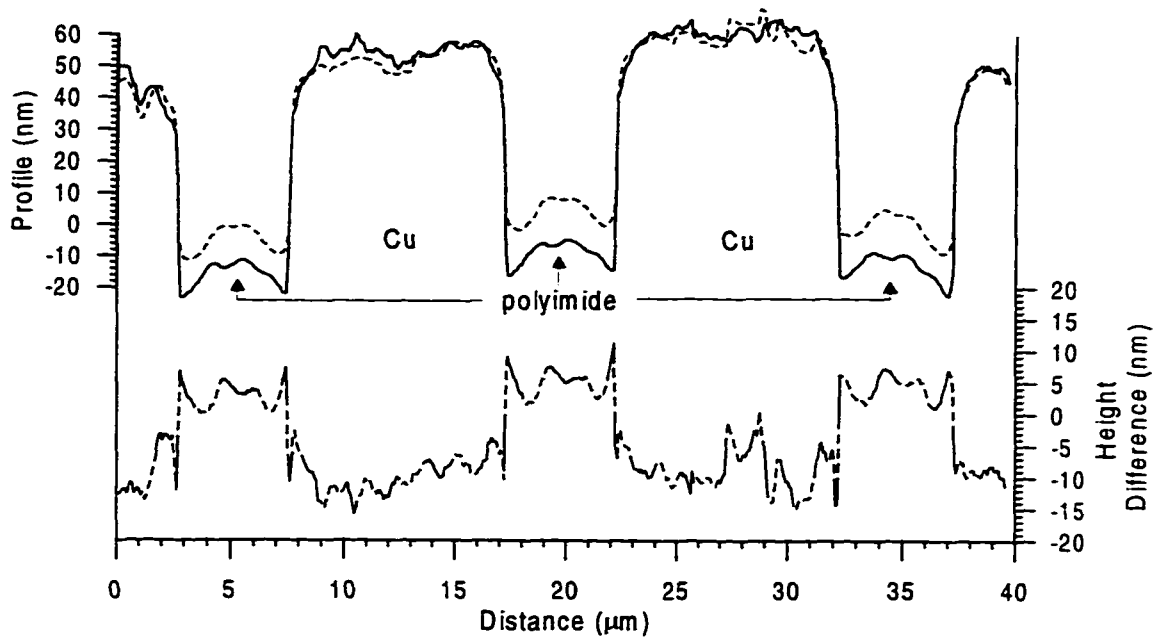
(a) 5 μm wide polyimide and 10 μm wide Cu lines
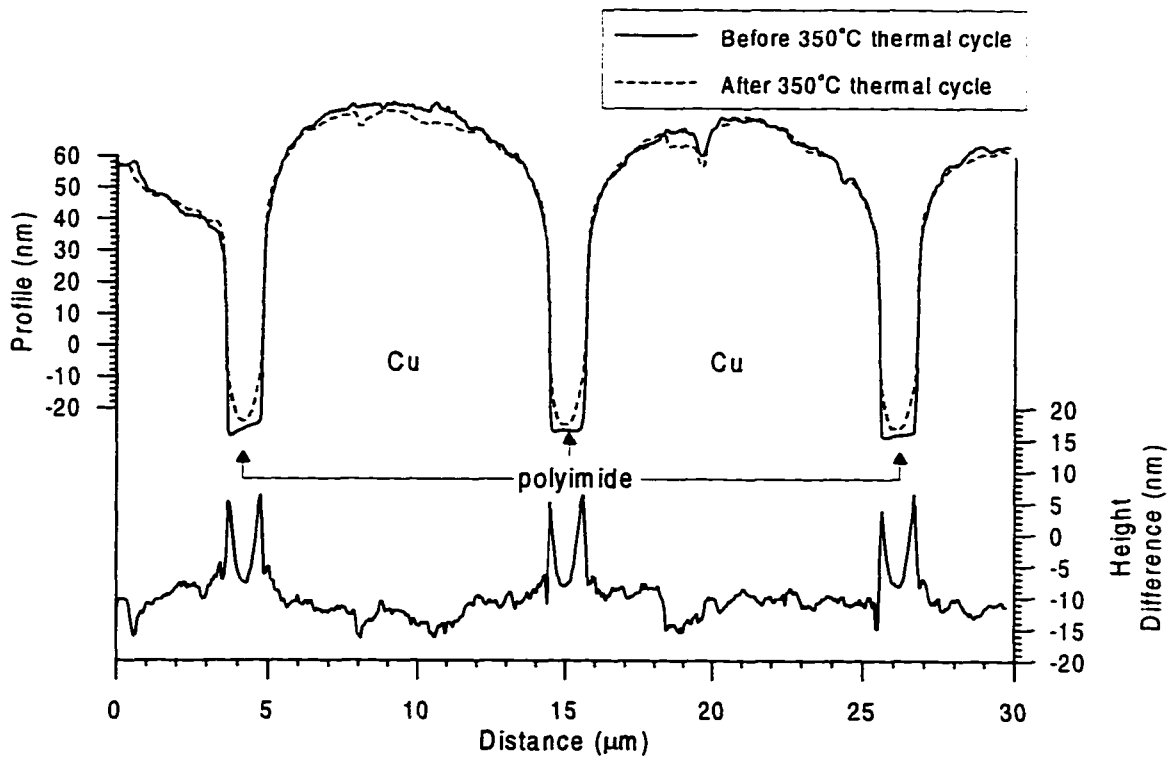
(b) 1.2 μm wide polyimide and 10 μm wide Cu lines

Figure 4-8. Deformation plots for 10 μm wide Cu lines in FPI-136 sample
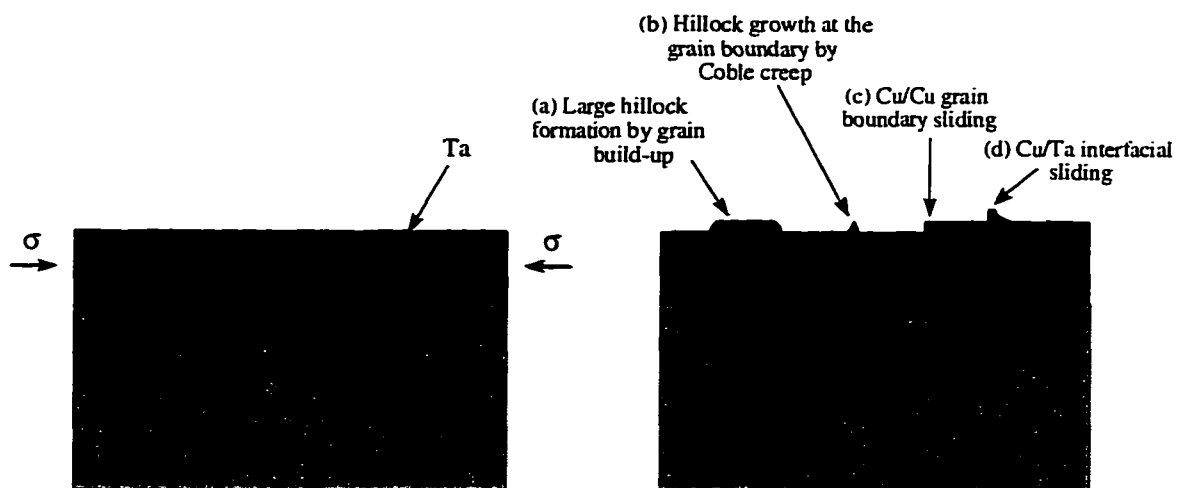
Figure 4-9. Stress-relaxation mechanisms in Cu/Ta/polyimide line arrays

4.3. Discussion

Figure 4-9 is a schematic summary of the deformation mechanisms observed on these structures. The in-plane deformation results from the in-plane stresses formed by the CTE mismatch between the Cu and the Si substrate. The out-of-plane deformation results from out-of-plane CTE mismatch between the polyimide, the Ta liner, and the Cu film. These deformation mechanisms include hillock formation from stress relaxation by Coble creep, hillock formation attributed to mass flow to grains with a lower in-plane elastic constant, Cu/Cu grain boundary sliding, and Cu/Ta interfacial sliding.

There are two noteworthy experimental observations that merit further discussion. They are:

- Sliding occurs at the Cu/Ta interface for 1 μm wide Cu lines but little or no sliding occurs at the Cu/Ta interface for 10 μm wide Cu lines.

67
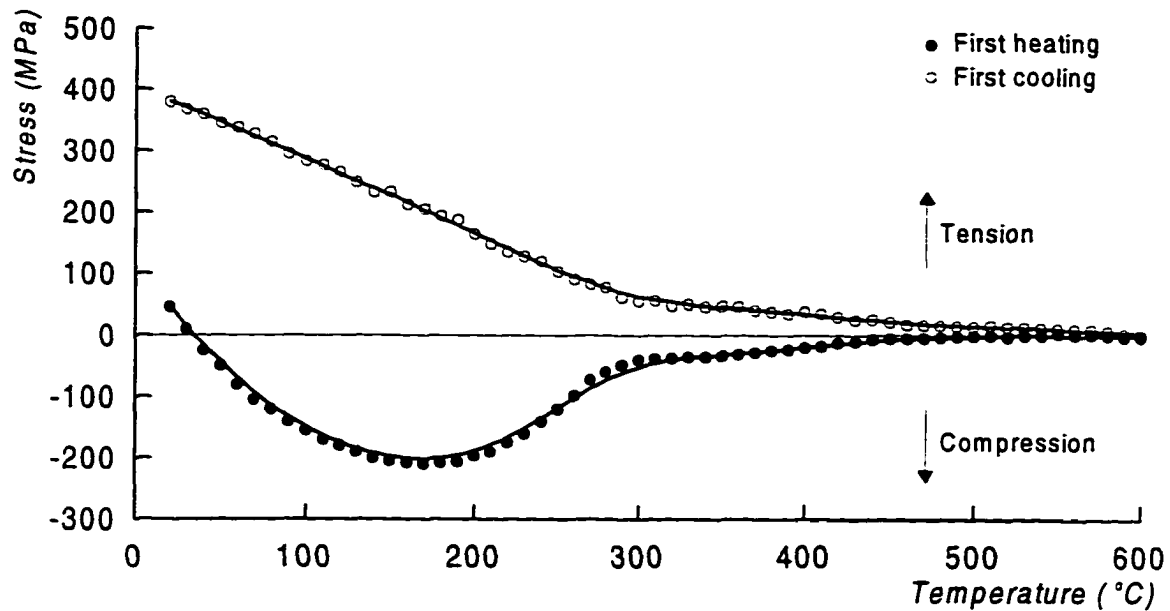
Figure 4-10. Typical Stress - Temperature plot for a 1 μm thick Cu film. (Adapted from Flinn[29])

· The magnitude of sliding decreases as the polyimide line width decreases. First, we will discuss the origin of the sliding and then we will discuss the dependence of the amount of sliding on width of the Cu and the polyimide lines.

4.4. Stress Relaxation Mechanisms in Blanket Cu Films

Figure 4-10 shows the biaxial stress in a 1 μm thick Cu film on a Si substrate subjected to a 600 °C thermal cycle as reported by Flinn.[29] The tensile stress initially present in the film is a result of cooling after deposition. On heating, the tensile stress decreases as the temperature approaches the deposition

68

temperature. Starting at about 150 °C, compressive stress develops and increases in magnitude until the temperature is about 200 °C. As the temperature is further increased, there is a drop in stress associated with stress relaxation. The stress remains extremely low during the rest of the heating cycle.

Stress relaxation in a thin epitaxial film can occur by various mechanisms, with different mechanisms dominant in different regimes of stress and temperature. The following deformation mechanisms[30] can be activated in a thin film polycrystalline material during a thermal cycle:

- Dislocation glide limited by either discrete obstacles or by lattice resistance.

- Dislocation climb and glide, which involves either lattice diffusion dominated (high temperature creep) or dislocation-core dominated (low temperature creep) power-law creep.

- Grain boundary sliding by lattice diffusion (Nabarro-Herring creep).

- Grain boundary sliding by boundary diffusion (Coble creep).

4.4-1. Low-temperature dislocation glide

Flow by glide motion of dislocations is possible below the ideal shear strength, provided an adequate number of independent slip systems are available. This motion is almost always obstacle-limited. It is the interaction of potentially mobile dislocations with other dislocations, with solute atoms,

69

precipitates, grain boundaries, or with the periodic friction of the lattice itself which determines the rate of flow and the yield strength. The obstacles fall into two broad classes: discrete obstacles which are bypassed individually by a moving dislocation (strong dispersoids or precipitates, for example) or cut by it (such as forest dislocations or weak precipitates); and extended, diffuse barriers to dislocation motion which are overcome collectively (a lattice-friction, or a concentrated solid solution). The strain rate for discrete-obstacle controlled plasticity is calculated by

$$\dot{\varepsilon} = \dot{\gamma}_0 \exp\left[-\frac{Q_g}{kT}\left(1 - \frac{\sigma}{\sqrt{3}\hat{\tau}}\right)\right]$$ (4.1)

where $\hat{\tau}$ is the shear strength at a temperature of 0 K, $\dot{\gamma}_0$ is a preexponential constant, k is Boltzmann's constant, Q_g is the activation energy for dislocation glide, and σ is applied stress. The strain rate is determined by the activation energy Q_g - it characterizes the total free energy required to overcome the obstacle without aid from external stress.

Thouless et al.[31] measured the stress in a 1 μm thick Cu film with a grain size of about 1 μm subjected to a 25 °C - 450 °C - 25 °C thermal cycle. They analyzed their results using classical creep models to determine which mechanism was dominant in a given temperature range. It was found that if yield by low temperature plasticity is activated, it can only occur at the lowest temperatures (< 100 °C) and highest stress (>250 MPa).

70

4.4-2. Power-law creep by dislocation climb and glide

At high temperatures, dislocations acquire a new degree of freedom: they can climb as well as glide. If a gliding dislocation is held up by discrete obstacles, a little climb may release it, allowing it to glide to the next set of obstacles where the process is repeated. The glide step is responsible for almost all of the strain, although the average velocity is determined by the climb step. The important feature that distinguishes this mechanism from those of the previous section is that the rate-controlling process, at an atomic level, is the diffusive motion of single atoms or vacancies to or from the climbing dislocation, rather than the activated glide of the dislocation itself.

Above $0.6T_M$ climb is generally controlled by diffusion from the dislocations through the lattice. Diffusion along the dislocation cores contributes significantly to the overall diffusive transport of matter, and sometimes becomes a dominant mechanism at lower temperatures. The strain rate equation for power-law creep:

$$\dot{\varepsilon} = \frac{A D_{\text{eff}} G b}{kT}\left(\frac{\sigma}{\sqrt{3}G}\right)^n$$
$$D_{\text{eff}} = D_v\left[1+\frac{10 a_c}{b^2}(\sigma/\mu)^2\frac{D_c}{D_v}\right]$$

(4-2)

where D_v is the lattice diffusion coefficient, D_c the core diffusion coefficient, μ is the shear modulus which is assumed to be temperature dependent, b is an appropriate Burgers vector, a_c is the cross-sectional area of the dislocation

71

core in which fast diffusion is taking place, A and n are empirical fitting parameters, n varying from 3 to 10. The above equation is really two strain rate equations. At high temperatures and low stresses, lattice diffusion is dominant. At lower temperatures, or higher stresses, core diffusion becomes dominant, and the strain rate varies as σ^{n+2} instead of σ^n.

As reported by Thouless et al.,[31] during the 25 °C - 450 °C - 25 °C thermal cycle of 1 μm thick Cu films, deformation by lattice diffusion was found to be negligible. Creep by temperature-assisted dislocation motion was important at intermediate temperatures and determined the value of the maximum compressive stress.

4.4-3. Diffusional flow

A stress changes the chemical potential, φ, of atoms at the surfaces of grains in a polycrystal. A hydrostatic pressure changes φ everywhere by the same amount so that no potential gradients appear; but a stress with a deviatoric component changes φ on some rain surfaces more than on others, introducing a potential gradient, $\Delta\varphi$. At high temperatures this gradient induces a diffusive flux of matter through and around the surfaces of the grains, and this flux leads to strain, provided it is coupled with sliding displacements in the plane of the boundaries. Most models of the process (Nabarro[32], Herring[33], Coble[34], Raj and Ashby[35]) assume the flux is diffusion-controlled. If both lattice and grain boundary diffusion are permitted, the strain rate

72

equation for diffusional flow is:

$$\dot{\varepsilon} = \frac{42\sigma\Omega}{kTd^2} D_{\text{eff}}$$

$$D_{\text{eff}} = D_v\left[1 + \frac{\pi\delta}{d}\frac{D_b}{D_v}\right] \qquad (4.3)$$

Here d is grain size, D_b the boundary diffusion coefficient, δ the effective thickness of the boundary, and Ω is the atomic or ionic volume. Like the equation for climb-controlled creep, it is really two equations. At high temperatures, lattice diffusion controls the strain rate; the resulting flow is known as Nabarro-Herring creep and its rate scales as D_v/d^2. At lower temperatures, grain-boundary diffusion takes over; the flow is then called Coble creep, and scales as D_b/d^3. Coble creep is more sensitive to grain size than Nabarro-Herring creep. Thus, even though both forms of creep are favored by high temperature and low stress, it is expected that Coble creep will dominate the creep rate in very fine grained materials.

In the aforementioned 25 °C - 450 °C - 25 °C thermal cycle experiment on 1 μm thick Cu films with approximately 1 μm grains,[31] it was found that for temperatures above 300 °C, creep by grain-boundary diffusion was the dominant deformation mechanism.

73
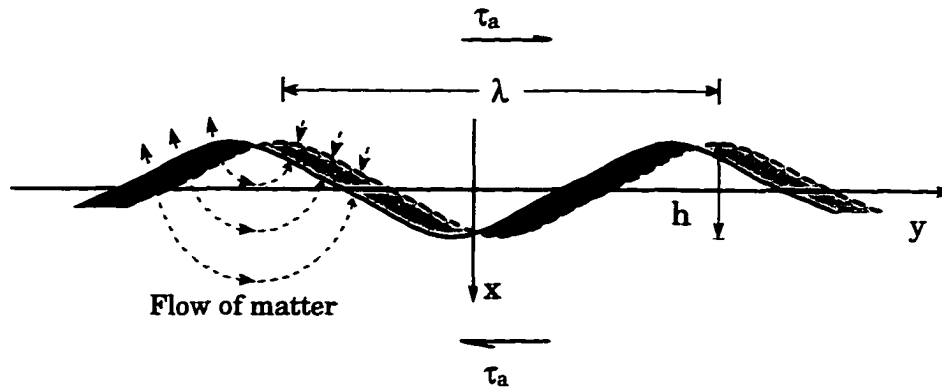
Figure 4-11. Steady-state sliding with diffusional accommodation. (Adapted from Raj and Ashby[35])

4.5. Mechanism of Interfacial Sliding

Out-of-plane shear stresses on the vertical interfaces can relax by diffusion accommodated grain boundary sliding between the Cu and the Ta. Raj and Ashby[35] have modeled diffusion accommodated grain boundary sliding for different interface shapes. For a sinusoidal interface of wavelength λ and amplitude $h/2$ subjected to a uniform shear stress τ_a, the steady-state, diffusion-controlled sliding rate, $\dot{U}_{Cu-Cu}$, is given by

$$\dot{U}_{Cu-Cu} = \frac{8}{\pi} \frac{\tau_a \Omega}{kT} \frac{\lambda}{h^2} D_v \left\{ 1 + \frac{\pi \delta}{\lambda} \frac{D_b}{D_v} \right\} \tag{4-4}$$

where h is the total height of the boundary shape, as shown in Figure 4-11. Here τ_a is the applied shear stress resolved on the boundary, Ω the atomic volume, D_v the bulk self-diffusion coefficient, D_b that for boundary diffusion, δ the thickness of the grain-boundary diffusion path, and λ is the periodicity of the roughness of the boundary. Relative displacement, i.e. grain boundary

74

sliding, of the upper and lower regions necessitates mass transfer. The mass transfer can be produced by volume diffusion near the grain boundary, by grain-boundary diffusion, or by both mechanisms. The mass transfer is driven by vacancy concentration gradients in the same manner that diffusional creep is driven. It should be noted that as the boundary becomes more irregular, i.e., as the ratio h/λ increases, more volume must be displaced per unit sliding displacement.

The above model applies to interfaces between identical materials. The temperature in the imidization cycle is too low for substantial diffusion to occur in the Ta liner (melting temperature of Ta is almost 3000 °C as opposed to 1083 °C for Cu). Therefore, only Cu atoms or vacancies take part in the diffusion flow to accommodate the shear component of stress. That is why the sliding rate at the Cu/Ta interface will be approximately half that for Cu/Cu interfaces:[36]

$$\dot{U}_{Cu-Ta} \approx \frac{1}{2} \dot{U}_{Cu-Cu} \qquad (4\text{-}5)$$

Shear stresses of 250-350 MPa on the Cu/Ta interface were estimated from a linear elastic, plane strain finite element model of 1 μm thick Cu/Ta/polyimide line arrays on the Si substrate subjected to heating from room temperature to 350 °C. The sliding at the Cu/Ta interface will occur at a rate of about 6 - 8 nm/sec for stresses of 250 - 350 MPa and an interface roughness of 1 nm. The sliding rate for an interface with a 10 nm interfacial

75

roughness (an upper limit for a 20 - 50 nm thick Ta liner) is 0.06 - 0.08 nm/sec at 350 °C. The sample spends 200 minutes in the high temperature range (300 - 350 - 300 °C at 2 °C/minute). During this period, the roughest interface can slide 12-16 nm. Clearly, the sliding rate is sufficient to relax shear stresses in the time scale of the thermal cycle.

The sliding at the Cu/Ta interface does not completely reverse on cooling because the minimum temperature for diffusional interfacial sliding is higher than the temperature corresponding to the zero shear stress at the interface in the time scale of a thermal cycle. Since the Ta cannot plastically deform at these stresses and temperatures, it elastically expands with the polyimide on heating and elastically contracts on cooling.

4.5-1. Effect of Cu line width on interfacial sliding

The difference in the amount of sliding between 1 μm and 10 μm wide Cu lines is attributed to Cu/Cu interfacial sliding instead of Cu/Ta. The schematic of this effect is shown in Figure 4-12. The 1 μm wide Cu lines typically have a bamboo structure - one grain wide with the grain boundary perpendicular to the interface. The wider lines are polycrystalline. As stated earlier, the Cu/Cu sliding rate is approximately twice as fast as the Cu/Ta sliding rate for the same shear stress. It is proposed that stress relaxation by Cu/Cu grain sliding at the grain boundaries parallel to the Cu/Ta interface is more rapid than Cu/Ta interfacial sliding. The fact that the deformation of

76
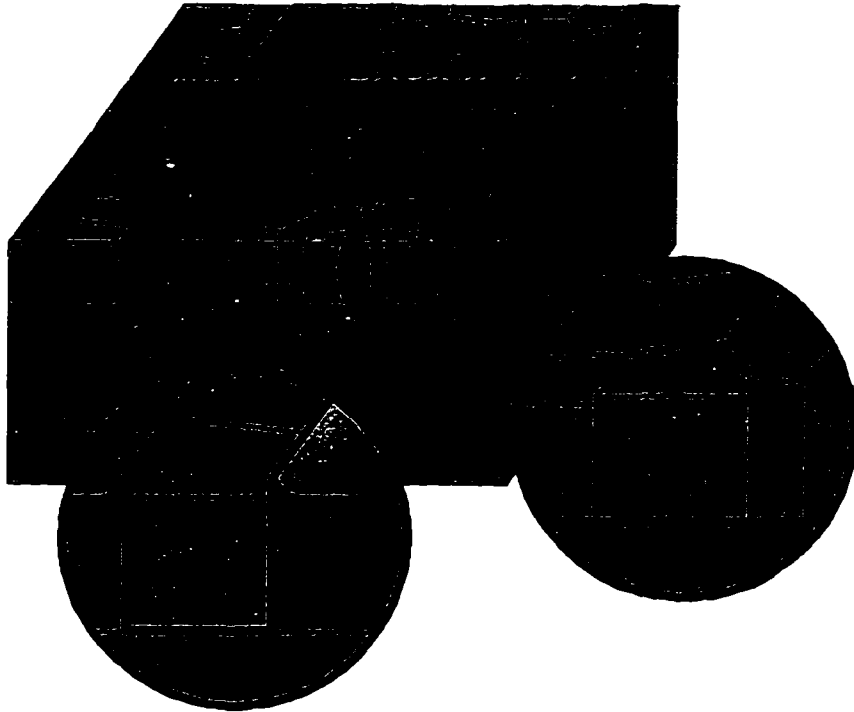
Figure 4-12. Diffusion accommodated grain boundary sliding in narrow and wide Cu lines. In wider lines, which have grain boundaries parallel to the Cu/Ta interface, Cu-Cu grain boundary sliding takes place.

the wide Cu lines exhibits a concave up curvature also supports this proposal.

Thus, the wider, polycrystalline Cu lines suppress diffusional sliding at the Cu/Ta interface by providing an alternate path for more rapid stress relaxation.

4.5-2. Effect of polyimide line width on sliding

It was previously shown that the thermal expansion of the polyimide lines 1 μm wide or less was more constrained. This was attributed to the creation of a damage zone from the reactive ion etching used to define the circuit pattern. Therefore, it is expected that the narrower polyimide lines will be subjected to lower shear stresses and would exhibit less sliding. This is

77

consistent with the observations summarized in Table 4-1 for the FPI-135. For each Cu line width, the magnitude of sliding was less for the narrower polyimide lines.

4.5-3. *Effect of polyimide CTE on the magnitude of sliding*

We previously used the AFM to determine the out-of-plane coefficients of thermal expansion (CTE) for HDICs fabricated with two polyimides, FPI-135 and FPI-136. It was found that the CTE of the FPI-135 polyimide ($\alpha_{FPI-135}$ = 260 ppm/K) is almost twice as high as that of the FPI-136 polyimide ($\alpha_{FPI-136}$ = 150 ppm/K) for 25 °C - 100 °C temperature range. Therefore, we expected the amount of Cu/Ta sliding to be greater for the samples with the higher CTE dielectric, i.e. the FPI-135 polyimide. Since the surface of the Cu was unstable for the FPI-136 samples, we were not able to either support or disprove another stated expectation about the Cu/Ta sliding being greater in the FPI-135 sample because of the changes in the Cu surface in the FPI-136 sample.

4.6. Summary of Experimental Observations

Thermomechanical deformation of 1 μm thick Cu/Ta/polyimide high density interconnect structures on a Si substrate as a result of 350 °C thermal cycle was observed with the AFM. It was found that in addition to the "classical" stress relaxation mechanism characteristic for blanket thin films,[30] diffusion accommodated sliding at the Cu/Ta interface also contributes to relaxation of

78

the out-of-plane shear stresses. The amount of the Cu/Ta interfacial sliding strongly depends on the width of the Cu lines. More Cu/Ta sliding was observed at the interface with the narrow (1 μm wide) Cu lines. This was attributed to the ability of the wider Cu lines (10 μm), which have several grains across the line, accommodate for the stresses by other mechanisms, such as Cu/Cu grain sliding at the grains parallel to the Cu/Ta interface. The secondary factor that affects the amount of the Cu/Ta sliding is the wiath of the adjacent polyimide lines. The thermal expansion of the narrow (1 μm) polyimide lines is more constrained which results in lower interfacial shear stresses and in less Ta sliding at the neighboring Cu/Ta interface. No sliding was detected at the Ta/polyimide interface.

4.7. Finite Element Analysis of Interfacial Sliding

4.7-1. Purpose of finite element analysis of interfacial sliding

Cu/polyimide high density interconnects experience temperatures of 350 – 400 °C during the polyimide imidization step of the fabrication process, as described on page 7. As was shown in the previous sections, deformation of high density interconnects becomes highly heterogeneous during the room temperature to 350 °C thermal cycle. Cu grain boundary sliding, Cu grain extrusion, Coble creep, and Cu/Ta interfacial sliding were observed experimentally. When multilevel interconnect structures are manufactured and the existing layers are subjected to the 350 °C thermal cycle, these

79

heterogeneous deformation mechanisms can cause mechanical failure, delamination of interlayer dielectric and delamination of the dielectric at vertical interfaces. Many researchers have studied stress distribution in high density interconnects using finite element analysis[37,38] to understand the driving force for failures that have been observed, but they assumed uniform inelastic deformation. Our experimental evidence suggests that these structures deform in more complex manner, and more accurate results will be achieved if heterogeneous deformation is included in the models. The following sections describe a first attempt to develop a Cu/Ta sliding interface model as a first step toward incorporating of heterogeneous nature of HDIC deformation into finite element modeling.

4.7-2. Finite element analysis implementation

Out of a variety of features in the high density interconnect samples, the line arrays were selected for analysis because their behavior could be simulated by a less computationally demanding two-dimensional generalized plane strain finite element model. A survey of different manufactures of commercial FEA packages indicated that suitable sliding interface elements are not available in their libraries. To overcome this problem one can utilize user subroutines supported by most of the packages, which allow inputting of a power law constitutive creep data. In the MARC/Mentat finite element program, a user can specify in the following form:

80

$$\dot{\bar{\varepsilon}}^c = A\,\bar{\sigma}^m\,\bar{\varepsilon}^n\,T^p\left(qt^{q-1}\right) \qquad (4\text{-}6)$$

where $\dot{\bar{\varepsilon}}^c$ is equivalent creep strain rate, and $\bar{\sigma}, \bar{\varepsilon}^c$, T and t are equivalent stress, equivalent creep strain, temperature and time, respectively. Therefore, an existing power law creep constitutive material model was utilized to create a heterogeneously deforming interface. It was proposed that by making the sliding interfacial layer thin, the majority of the deformation would be restricted to occur only in the plane of the interface. The behavior of a thin interfacial sliding layer has been modeled by Raj and Ashby,[35] and the steady-state, diffusion-controlled shear strain rate, is given by

$$\dot{\gamma} = A\frac{\tau_a\Omega}{kT}\frac{1}{h^3}\left[\lambda D_{0v}\exp\left(-\frac{Q_v}{kT}\right)+\pi\delta D_{0b}\exp\left(-\frac{Q_b}{kT}\right)\right] \qquad (4\text{-}7)$$

The above model applies to an interface between identical materials and assumes that both sides of the interface take part in the sliding. As discussed in section 4.4-3, it was proposed that only Cu atoms contribute to the sliding at the Cu/Ta interface. This is why Cu material properties shown below were used for the interfacial layer, and the scaling coefficient $\frac{1}{2}A$ was used instead.

81

Material properties	Copper
Crystallographic and thermal data Atomic volume, Ω (m^3) Burgers vector, b (m)	1.18 x 10^{-29} 2.56 x 10^{-10}
Lattice diffusion Pre-exponential, D_{0v} (m^2/s) Activation energy, Q_v (kJ/mole)	2 x 10^{-5} 197
Boundary diffusion Pre-exponential, δD_{0b} (m^3/s) Activation energy, Q_b (kJ/mole)	5.0 x 10^{-15} 104

Table 4-2. Diffusion coefficients for Cu[39]

4.7-3. Calibration of sliding interface elements

Before the described interfacial elements can be used in a model, constant A in equation (4-7) and the thickness of the layer have to be calibrated. This was done by generating a 1 nm thick interfacial layer in a FEA program, and applying a constant shear stress along the interface of the layer. Then the deformation of the interfacial layer from the finite element analysis was compared to the values calculated from Raj and Ashby model. The same procedure was repeated for a 10 nm thick interfacial layer. The constant A used in the finite element model was adjusted until the good match between the deformation predicted by FEA and equation (4-7) was achieved. Figure 4-13 shows the results of this comparison.
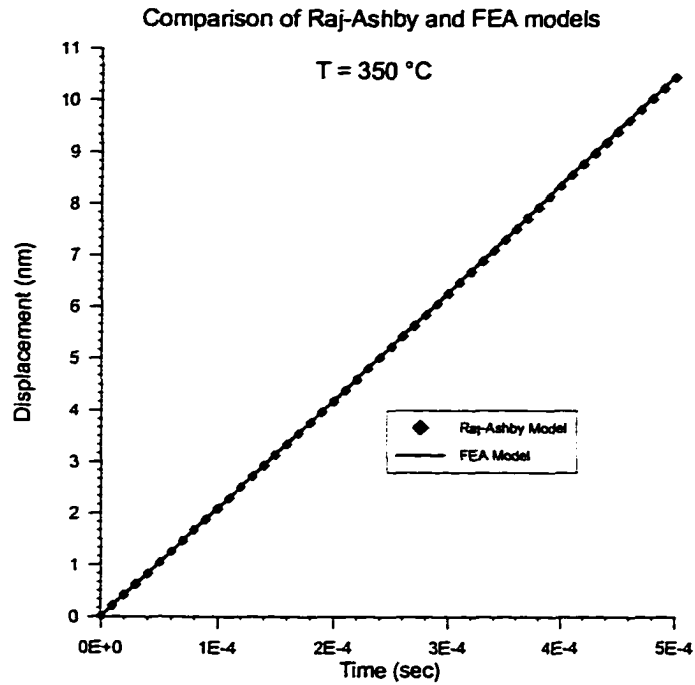
Figure 4-13. Comparison of Raj-Ashby and FEA models after calibration of scaling constant in equation (4-7)

It was found, that even though the sliding of interfacial layers of different thickness, predicted by the finite element model, matched the deformation derived from equation (4-7), the 1 nm thick layer performed much better in modeling the deformation in the direction normal to the interface. Significantly less deformation in the 1 nm thick interfacial layer occurred out of the plane of applied shear stress, whereas the 10 nm thick layer also exhibited some deformation in the normal direction. Therefore, the 1 nm thick interfacial sliding layer was chosen for the model.

Finally, the finite element model of a Cu/Ta/polyimide line array was constructed. The width of the Cu line was 5 μm, the polyimide − 10 μm, and

the width of the Ta liner was 30 nm. The interface between the Cu and the Ta liner was modeled by the 1 nm thick interfacial sliding elements discussed above. Material constants for Cu, polyimide and Ta that are listed in Table 3-2 on page 40, Table 3-3 on page 41 and Table 4-2 on page 82 were used in the model. Initially, it was proposed to simulate the imidization thermal cycle of this structure: heating from room temperature to 350 °C and cooling back to room temperature at a 2 °C/min rate. This approach turned out to be very computationally intensive, and it was suggested, as a first step toward studying more complex behavior, to study stress relaxation at Cu/Ta interface at 5 different temperatures. The structures were instantly heated from room temperature to 50 °C, 100 °C, 200 °C, 250 °C, and 350 °C, and the shear stress at the interface was calculated as a function of time in all five simulations. This approach allowed us to see if the introduced sliding interfacial element was able to model the desired behavior in a simple physical situation.

4.7-4. Finite element analysis results

The deformation maps of the Cu/Ta/polyimide line array with a Cu/Ta sliding interface are shown in Figure 4-14. In this case the structure was heated instantaneously from room temperature to 250 °C, which resulted in thermal expansion of the polyimide as shown in Figure 4-14(a). Then the structure was held at this temperature, and stress and deformation were calculated as

84
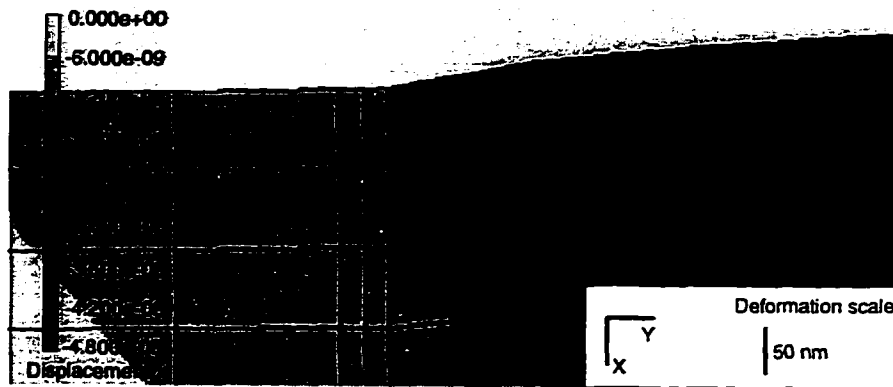
(a) Immediately after heating from room temperature to 250 °C
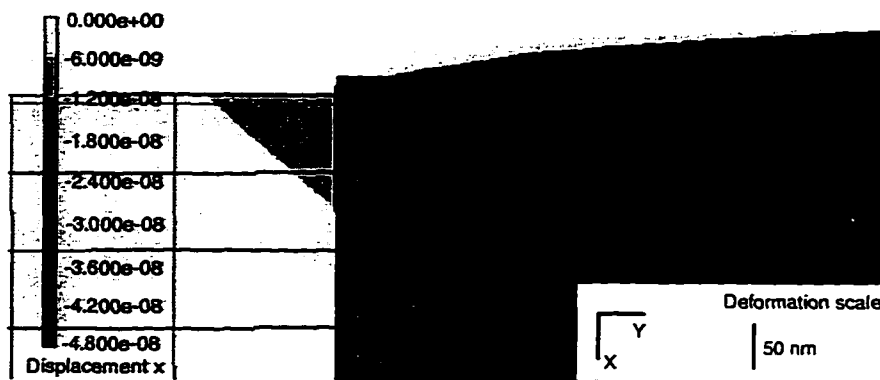
(b) 0.5 seconds after the heating

Figure 4-14. Finite element analysis model prediction of sliding at Cu/Ta interface.

a function of time. Figure 4-14(b) shows the interface region of the model less than 1 second later, when the shear stress started to relax and noticeable sliding at the Cu/Ta interface took place.

The shear stresses at the interface calculated for stress relaxation simulations at 50 °C and 350 °C were plotted as a function of time, as shown in Figure 4-15. Due to the length of time it took to consider a single

85
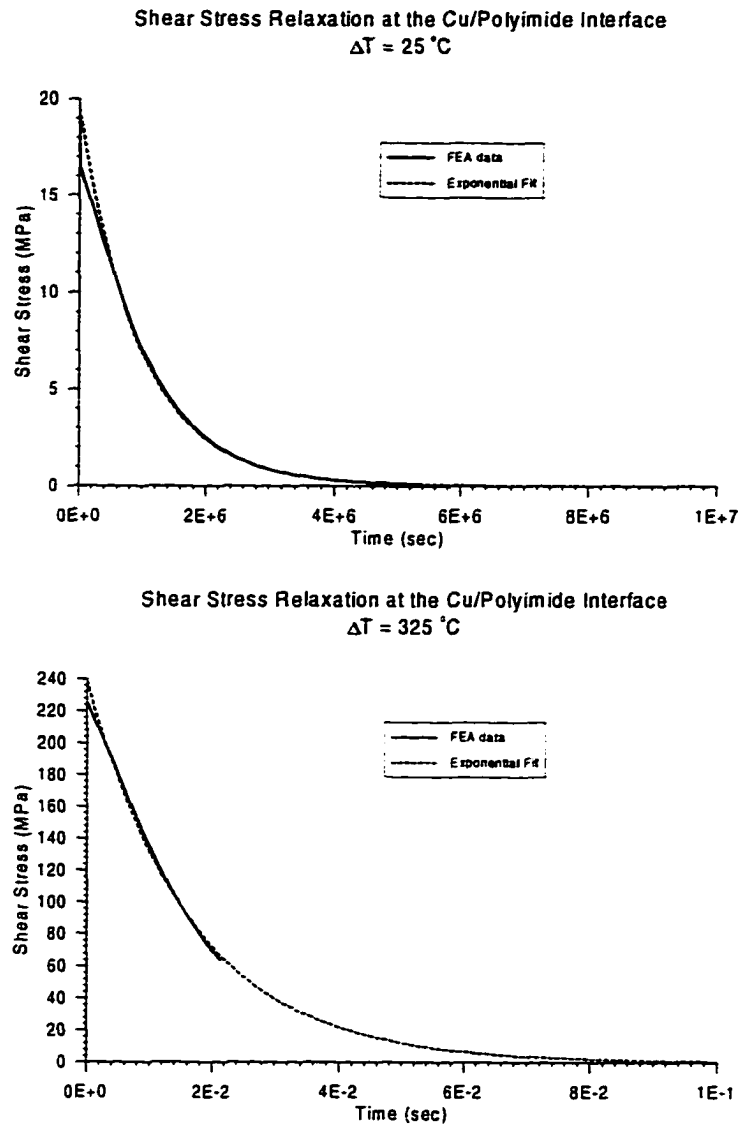
Figure 4-15. Stress relaxation plots at different temperatures as calculated by finite element model

temperature simulation (3 days on a SGI workstation with a 100 MHz MIPS processor and 192 Mb of RAM), the finite element stress relaxation simulations were not carried out for the whole time period necessary to completely relax the stress, but the data was sufficient to extrapolate the stress-temperature dependence. As can be seen in Figure 4-15, both stress-temperature curves are very well represented by exponential functions. This

86
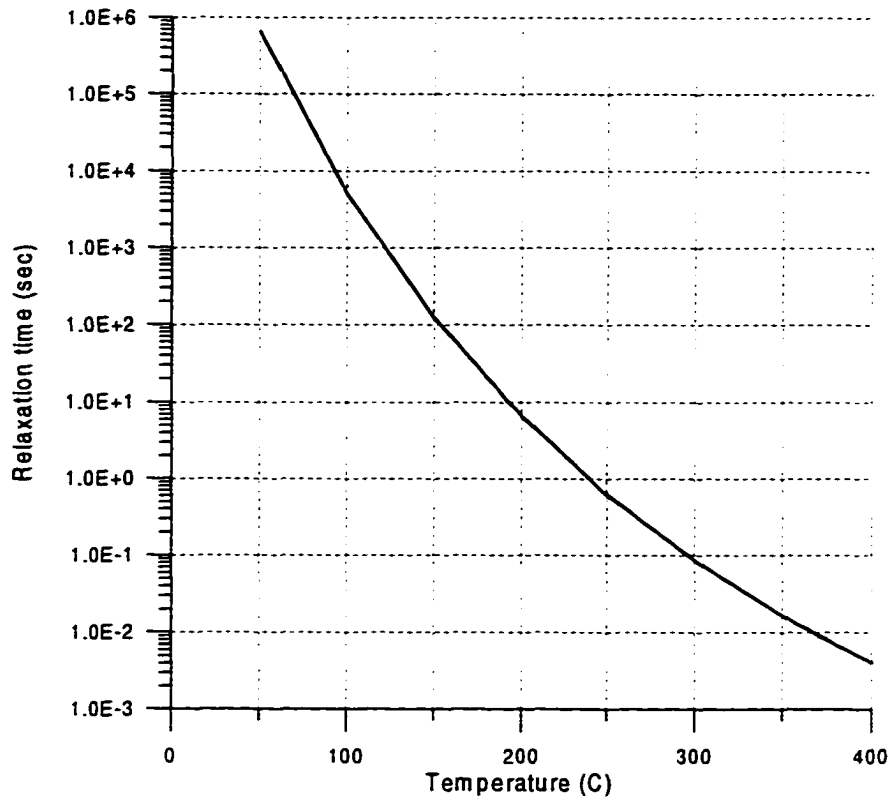
Figure 4-16. Stress relaxation times at different temperatures as predicted by finite element analysis

exponential dependence of stress on relaxation time was observed for all considered temperatures.

Based on the exponential extrapolation functions, the time necessary to relax the shear stresses at the interface was plotted as a function of temperature, as shown in Figure 4-16. When the temperature of the high density interconnect is raised to 50 °C, it takes about 11 days to relax the shear stresses at the Cu/Ta interface, whereas at 350 °C the stress will relax immediately, in only 0.016 seconds.

87

The finite element analysis described in the above sections was only a first step toward incorporating of heterogeneous deformation mechanisms into numerical models, and many important aspects of it were left out of consideration. More complex models should include sliding at Cu/Ta horizontal interface, stress relaxation by grain boundary sliding, etc. Also, it would be important to analyze the high temperature stress distribution of Cu/Ta/polyimide structures capped with an interlayer dielectric.

4.8. Finite Element Analysis Summary

A finite element model was created to analyze the sliding at the Cu/Ta interface of the HDICs as a result of the 350 °C thermal cycle. The Raj-Ashby model of interfacial sliding was used to calibrate the behavior of the sliding interface elements for the numerical analysis. Stress relaxation time as a function of temperature was derived from the finite element analysis results. This data showed significant differences between the amount of time it takes to relax stress at different temperatures. Whereas at 50 °C, interfacial shear stress will relax after about 11 days, at 350 °C this process will take a fraction of a second. The model has shown that stress relaxation in high density interconnects is a very rapid process, and this has to be kept in mind when manufacturing and storing these devices. Even though this model was a first step toward studying more complex behavior, and many aspects of heterogeneous deformation were not considered, it set up a new strategy in modeling of stresses in high density interconnects. To obtain more accurate

88

results, other heterogeneous deformation mechanisms, such as grain boundary sliding, Coble creep and sliding at horizontal interfaces have to be included in finite element models.

89

CHAPTER 5

CONCLUSION

A new technique for out-of-plane thermal expansion coefficient measurement of 1 μm thick polyimide films was developed. Using atomic force microscopy the CTE was estimated from relative height changes between the parallel Cu and polyimide lines from room temperature to 97 °C.

It was shown that the thermomechanical behavior of polyimide strongly depends on polyimide line with width. Narrow ($\leq$ 1 μm wide) lines typically show less thermal expansion than wider lines. This is attributed to change of polyimide properties at the Cu/polyimide interface as a result of the reactive ion etching (RIE). When the width of a polyimide line approaches the width of the "damage zone", the thermomechanical response of the structure becomes affected by the properties of the damage zone.

Buckling of the nitride cap was observed to result in waviness on the surface of the capped BPDA-PDA polyimide. The nitride cap is deposited at elevated temperature, and on cooling the CTE mismatch between Si_3N_4 the polyimide leads to formation of residual compressive stress in the nitride film. This

90

stress results in buckle formation on the surface of the cap. The buckle amplitude, wavelength, and position changed on cooling. Usually the buckles disappeared on heating and reappeared on cooling.

Thermomechanical deformation of 1 μm thick Cu/Ta/polyimide high density interconnect structures on a Si substrate resulted from room temperature – 350 °C – room temperature thermal cycle was observed with the AFM. It was found that in addition to the "classical" stress relaxation mechanism characteristic for blanket thin films[30] diffusion accommodated sliding at the Cu/Ta interface also contributes to relaxation of the out-of-plane shear stresses. The amount of the Cu/Ta interfacial sliding strongly depends on the width of the Cu lines. More Cu/Ta sliding was observed at the interface with the narrow (1 μm wide) Cu lines. This was attributed to the ability of the wider Cu lines (10 μm), which have several grains across the line, accommodate for the stresses by other mechanisms, such as Cu/Cu grain sliding at the grains parallel to the Cu/Ta interface. The secondary factor that affects the amount of the Cu/Ta sliding is the width of the adjacent polyimide lines. The thermal expansion of the narrow (1 μm) polyimide lines is more constrained which results in lower interfacial shear stresses and in less Ta sliding at the neighboring Cu/Ta interface. No sliding was detected at the Ta/polyimide interface.

91

A finite element model was created to analyze the sliding at the Cu/Ta interface of the HDICs as a result of the 350 °C thermal cycle. Sliding interfacial elements were generated based on the Raj-Ashby model of diffusion accommodated grain boundary sliding. This allowed using commercially available finite element packages. The amount of sliding calculated by the model is comparable with the experimental observations. It was found that the stress relaxation times vary strongly on the temperature of the thermal cycle. Even though not all the stress relaxation mechanisms were included in the model, it was shown that more accurate results can be obtained by finite element modeling of high density interconnects if heterogeneous deformation is considered. This model was a first step toward more complex numerical investigation of thermal deformation of HDICs.

REFERENCES

1. M. Small and D.J. Pearson, *IBM J. Res. Develop*, 34(6), 419 (1990)

2.. J.M.E. Harper, E.G. Colgan, C-K. Hu, J.P. Hummel, L.P. Buchwalter, and C.E. Uzoh, *MRS Bulletin* XIX(8), 23 (1994)

3. D. Edelstein, *Proc. SPIE*, 1389, 352 (1990)

4. S. Herminghause, D. Boese, D. Yoon, B. Smith, *Appl. Phys. Lett.* 59, 1043 (1991)

5. S.T. Chen and H.H. Wagner, *J. Electron. Mater.* 22(7), 797 (1993)

6. T.J.Licata, E.G. Colgan, J.M.E. Harper, and S.E. Luce, *IBM J. Res. Develop.* 39(4), 419 (1995)

7. F.B. Kaufman, D.B. Thompson, R.E. Broadie, M.A. Jaso, W.L. Guthrie, D.J. Pearson, and M.B. Small, *J. Electrochem. Soc.* 138, 3460 (1991)

8. A.E.Feiring, B.C. Auman, E.R. Wonchoba, *Macromolecules* 26, 2779 (1993)

9. B.C. Auman, *Proc. 6th Meeting of The DuPont Symposium on Polyimides in Microelectronics*, May 1-3 (1995)

. K.C. Sheth, M.J. Chen and R.J. Farris, ANTEC'95 2671 (1995)

11. P. Zoller, P. Bolli, V. Pahud, and H. Ackerman, *Rev. Sci. Instrum.* 47(8), 948 (1976)

12. M.A. Maden and R.J. Farris, *Exp. Mech.* 31(2), 178 (1991)

13. G. Binnig, C.F. Quate and C. Gerber, *Phys. Rev. Lett.* 56, 930 (1986)

14. G. Meyer and N.M. *Appl. Phys. Lett.* 53, 2400 (1988)

15. *DimensionTM 3000 Scanning Probe Microscope Instruction Manual*, Digital Instruments, Inc.

16. D.Y. Yoon, W. Parish, L.E. Depero and M. Ree, *Mater. Res. Soc. Symp. Proc.* 227, 387 (1991)

17. M. Ree, K. Kim, S.H. Woo and H. Chang, *J. Appl. Phys.*, 81(2), 698 (1997)

18. H. Nomura and M. Asano, *Jpn. J. Appl. Phys.*, Part 1, 34, 6143 (1995)

19. K.C. Sheth, M.J. Chen and R.J. Farris, personal communication

20. P. Kofstad, *High-Temperature Oxidation of Metals*, (New York: John Wiley & Sons, 1966)

21. M. Ree, K. Kim, S.H. Woo and H. Chang, *J. Appl. Phys.* 81(2), 698 (1997)

22. N.S. Saha and L.-H. Chang, *Metallized Plastics 3: Fundamental and Applied Aspects*, ed. by K.L. Mittal, (New York: Plenum Press, 1992)

23. M.P. Zussman, S. Wood, L.C. Scala, J. Bartko and A. Vincenz, *J. Appl. Polym. Sci.* 35, 2183 (1988)

24. L.J. Matienzo, F. Emmi, D.C. Van Hart and T.P. Gall, *J. Vac. Sci. Technol.* A7, 1784 (1984)

25. D.V. Zhmurkin, T.S. Gross, L.P. Buchwalter, and F.B. Kaufman, *J. Electron. Mater.* 25(6), 976 (1996)

26. J.E. Sanchez, Jr., *Mat. Res. Symp. Proc.* 343, 641 (1994)

27. P.R. Besser, J.E. Sanchez, Jr., Brennan S., J.C. Bravman, G. Takaoka, and I. Yamada, *Mat. Res. Symp. Proc.* 343, 659 (1994)

28. R.A. Schwarzer and D. Gerth, *J. Electron. Mater.* 22 (6), 607 (1993)

29 P.A. Flinn, *J. Mater. Res.* 6 (7), 1498 (1991)

30. H.J. Frost in *Materials Reliability in Microelectronics II*, MRS Symp. Proc., 265 (1992)

31. M.D. Thouless, J. Gupta, and J.M.E. Harper, *J. Mater. Res.*, 8 (8), 1845 (1993)

32. F.R.N. Nabarro, *Report on a Conference on the Strength of Metals* (Phys. Soc. London) (1948)

33. C. Herring, *J. Appl. Phys.*, 21, 437 (1950)

34. R.L. Coble, *J. Appl. Phys.*, 34, 1679 (1963)

35. R. Raj, M.F. Ashby, *Metal. Trans.*, 2 (4), 1113 (1971)

36. R. Raj, personal communication

37. R.H. Lacombe; L.P. Buchwalter; K. Holloway, *J. Adhesion Sci. Technol.* 7, 1293 (1993)

38. J. Dolbow, M. Gosz, *Mech. of Materials* 23, 311 (1996)

39. H.J. Frost and M.F. Ashby, *Deformation-Mechanism Maps* (Pergamon, Oxford, 1982)